nature communications

Article

https://doi.org/10.1038/s41467-026-71659-7

SPNS2 exports sphingosine-1-phosphate and imports glucose

Received: 14 November 2025

Accepted: 25 March 2026

Cynthia Weigel[1], **Md Lokman Hossen**[2,6], **Ryan D. R. Brown**[1,7], **Can E. Senkal**[1], **Christopher D. Green**[1], **Jason Newton**[1,8], **Sumit Saha**[1], **Elisa N. D. Palladino**[1], **Bin Ni**[3], **Francesco S. Celi**[3,9], **Xianjun Fang**[1], **Frank D. Corwin**[4], **Huanyu Z. Li**[5], **David B. Sauer**[5], **Prem P. Chapagain**[2] & **Sarah Spiegel**[1]

Spinster homolog 2 (SPNS2) exports the bioactive sphingolipid metabolite sphingosine-1-phosphate (S1P) out of cells to regulate processes important for health and diseases. However, the molecular mechanism underlying SPNS2 transport functions and its precise physiological roles are not fully understood. Here, through a series of complementary approaches in mice, cellular assays, and particularly with in vitro cell-free binding and transport assays, we show that SPNS2 has antiporter-like activity, transporting S1P out of cells and glucose in. We demonstrate that SPNS2 directly binds glucose and transports it and identify key amino acid residues of SPNS2 involved in glucose engagement and import. Our data reveal that S1P, which enters from the cytosolic side of SPNS2 facilitates conformational changes, enabling extracellular glucose to move inward through the central cavity. Thus, we identify a mechanism that dynamically contributes to glucose homeostasis in response to metabolic and sphingolipid cues with clinical and pathophysiological implications.

Sphingosine-1-phosphate (S1P), a pleiotropic bioactive sphingolipid metabolite synthesized intracellularly by sphingosine kinases, is exported out of cells by the specific transporter, spinster homolog 2 (SPNS2), to regulate numerous processes important for health and diseases by binding to its receptors termed S1PRs[1]. S1P accumulates with overnutrition in mice and humans and has been implicated in obesity, diabetes, glucose homeostasis, and other metabolic diseases[2–4]. SPNS2, a member of the solute carriers (SLC) that belongs to the major facilitator superfamily (MFS)[5], is highly expressed on vascular and lymphatic endothelial cells. It facilitates the export of S1P into the bloodstream and lymph, thereby establishing the S1P gradient between circulation and tissues that directs lymphocytes trafficking[1,6,7]. SPNS2 is also expressed on other cells[8,9] and plays critical roles in cancer metastasis[10], the auditory system, ocular development[11], as well as inflammatory and autoimmune disorders[12]. Elucidating the molecular mechanisms governing S1P transport and SPNS2 functions are essential for understanding the complex balance between physiological homeostasis and disease development. In this work, we show that SPNS2 exhibits antiporter-like activity, exporting S1P out of cells while importing glucose in. We demonstrate that SPNS2 also directly binds glucose and identify key amino acid residues required for glucose recognition and uptake. Our findings reveal a mechanism linking SPNS2 to glucose homeostasis with important clinical and pathophysiological relevance.

---

[1]Department of Cellular, Molecular and Genetic Medicine, Virginia Commonwealth University School of Medicine, Richmond, VA, USA. [2]Department of Physics and Biomolecular Sciences Institute, Florida International University, Miami, FL, USA. [3]Department of Internal Medicine, Virginia Commonwealth University School of Medicine, Richmond, VA, USA. [4]Department of Radiology, Virginia Commonwealth University School of Medicine, Richmond, VA, USA. [5]Centre for Medicines Discovery, Nuffield Department of Medicine, University of Oxford, Oxford, UK. [6]Present address: Department of Physics, University of Barishal, Kornokathi, Barishal, Bangladesh. [7]Present address: School of Life Sciences, Keele University, Staffordshire, UK. [8]Present address: School of Life Sciences and Sustainability, Virginia Commonwealth University, Richmond, VA, USA. [9]Present address: Department of Medicine, UConn Health, University of Connecticut, Farmington, CT, USA. e-mail: cynthia.weigel@vcuhealth.org; sarah.spiegel@vcuhealth.org

Results

SPNS2 deletion in mice leads to dysglycemia

The high-confidence AlphaFold 2 (https://alphafold.ebi.ac.uk/) predicted structure of human SPNS2 (hSPNS2) in inward-facing conformation[13], which was recently validated by cryo-EM[14–16], shows the canonical MFS fold of 12 transmembranes comprised of N and C domains. Each domain is composed of six consecutive transmembrane helices. In accord with the view of the rocker-switch mechanism proposed for MFS transporters, it was suggested that movement of both the N and C domains modulates the translocation pathway of S1P[14,17]. ConSurf analysis (https://consurf.tau.ac.il/)[18] illustrated the high degree of evolutionary conservation derived from multiple sequence alignments of the SPNS2 proteins (Fig. 1a and Supplementary Fig. 1) that were mainly located within the MFS domain[17]. Pairwise alignments between the human genetic and protein sequences of several model organisms, including mice, rats, dogs, chicken, the non-human primate *Macaca mulatta*, the cow *Bos taurus*, *Xenopus*, and zebrafish showed 74–99% sequence identity (Fig. 1b), supporting the evolutionary and functional conservation of SPNS2.

Given the high level of structural and evolutionary conservation, we used *Spns2*$^{-/-}$ mice for elucidating the physiological functions of SPNS2. As expected of a S1P transporter, deletion of *Spns2* resulted in a significant decrease in circulating S1P levels in blood, plasma, and lymph fluid, consistent with some previous reports[12,19], and also increased tissue S1P levels in liver, lung, kidney and heart (Fig. 1c). Analysis of blood did not reveal any significant changes in pH, sodium, potassium, calcium, chloride, bicarbonate, lactate, or arterial base excess (Supplementary Fig. 2a), consistent with lack of effects on the transport activity of SPNS2 in cells by altering extracellular pH, or potassium or sodium concentrations[14,15] which suggested that SPNS2 is not a proton- or sodium-dependent transporter[14,15].

In *Spns2*$^{-/-}$ mice that have decreased levels of S1P in blood and lymph (Fig. 1c), glucose levels were significantly increased (Fig. 1d). Glucose levels were also increased in feces and urine (Fig. 1e). Conversely, in peripheral tissues of *Spns2*$^{-/-}$ mice, S1P was increased (Fig. 1c) whereas glucose was decreased (Fig. 1d, e). Although the absence of SPNS2 significantly decreased body weights, with reduced fat percentages (Fig. 1f), surprisingly, these mice consumed more food and water and had a positive energy balance, while their energy expenditure and locomotor activity did not significantly change compared to wild-type (WT) mice (Fig. 1e and Supplementary Fig. 2b). While hemoglobin levels were not altered, levels of glycated hemoglobin (HbA1c) were increased in *Spns2*$^{-/-}$ mice (Fig. 1h), suggesting long-lasting high blood glucose, possibly due to the increased food intake (Fig. 1g). Dysglycemia was associated with increases in levels of triglycerides, phospholipids, cholesterol and non-esterified fatty acids, albeit not all significantly (Supplementary Fig. 2c). In an oral glucose tolerance test (GTT), the most physiological route of glucose entry, *Spns2*$^{-/-}$ mice had rapid and high increases in blood glucose levels which quickly dropped with a similar area under the curve (AUC) as in WT mice (Fig. 1i). Oral glucose also increased S1P in plasma and lymph, while food deprivation decreased it (Supplementary Fig. 3a, b). Nevertheless, levels of the glucose uptake-regulating hormones insulin and glucagon as well as levels of thyroid hormones triiodothyronine (T3) and thyroxine (T4) were similar in both genotypes (Fig. 1j and Supplementary Fig. 3d, e).

We next utilized positron emission tomography (PET) and computed tomography (CT) scans to follow the dynamic distribution of the

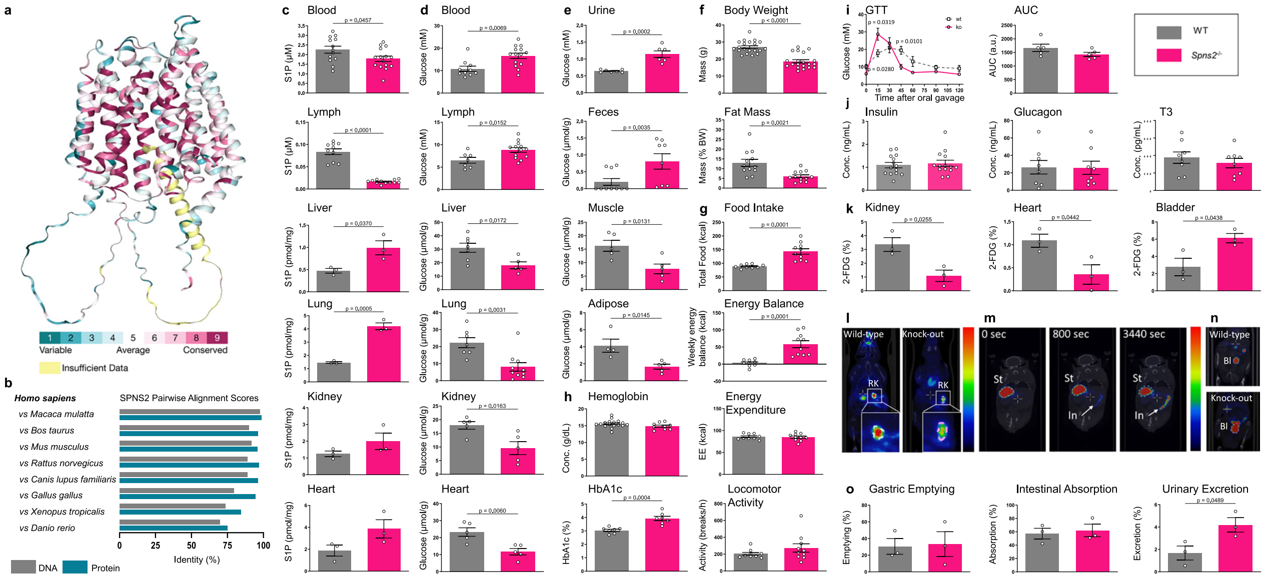

Fig. 1 | SPNS2 is evolutionary conserved, and its deletion leads to dysglycemia in mice. a ConSurf analysis of hSPNS2 protein. **b** Pairwise Alignment Scores for hSPNS2 protein and DNA sequences with putative homologs arranged according to the degree of sequence identity. **c** S1P levels in blood (n = 13, 15), lymph fluid (n = 10, 12), perfused liver, lung, kidney, heart (n = 3, 3). **d** Glucose levels in blood (n = 10,14), lymph fluid (n = 7, 13), perfused liver (n = 7, 5), lung (n = 7, 10), kidney (n = 5, 5), heart (n = 5, 5). **e** Glucose levels in urine (n = 7, 6), feces (n = 10, 8), tibialis anterior muscle (n = 5, 5), and gonadal adipose tissue (n = 4, 5). **f** Body weights (n = 20, 20). Body composition expressed as percentage of fat mass (n = 12, 12). **g** Food consumption, energy balance, energy expenditure, and locomotor activity (Beam breaks/h) determined with the PhenoMaster (n = 9,10; N = 3). **h** Blood hemoglobin concentration (n = 17, 9) and percentage of glycosylated hemoglobin, HbA1c (n = 7, 7). **i** Oral glucose tolerance test (GTT) and area under the curve (AUC) (n = 5, 5; N = 2). **j** Plasma levels of fasting insulin (n = 14, 14), glucagon (n = 8, 8) and thyroid hormone triiodothyronine (T3). Data are means ± s.e.m. **k–n** PET-CT imaging analysis of 2-FDG in *Spns2*$^{-/-}$ mice. PET tracer 2-FDG (270–550 μCi) was gavaged prior to anesthetization of WT or *Spns2*$^{-/-}$ mice for PET-CT scans. (n = 3, 3, N = 2). **k, l** At 60 min, tracer activity of target organs was quantified in volumes of interest (VOI). Data are percentage of whole-body activity for the right kidney (RK), heart, and bladder (Bl). **l** Coronal sections (0.4 mm thick) of PET images are presented according to a spectral scale for tracer activity, from red (highest), to green (intermediate), to blue (lowest). **m** The distribution of 2-FDG in representative WT at the specified times following gavage is shown to demonstrate the assessment of gastric emptying and intestinal absorption. St, stomach; In, intestines. **n** Representative images of the VOI in bladder to determine % of urinary excretion. **o** % of urinary excretion, gastric emptying and intestinal absorption. Data are means ± s.d. Two-tailed unpaired t-test. Source data are available for this figure in the Source Data file.

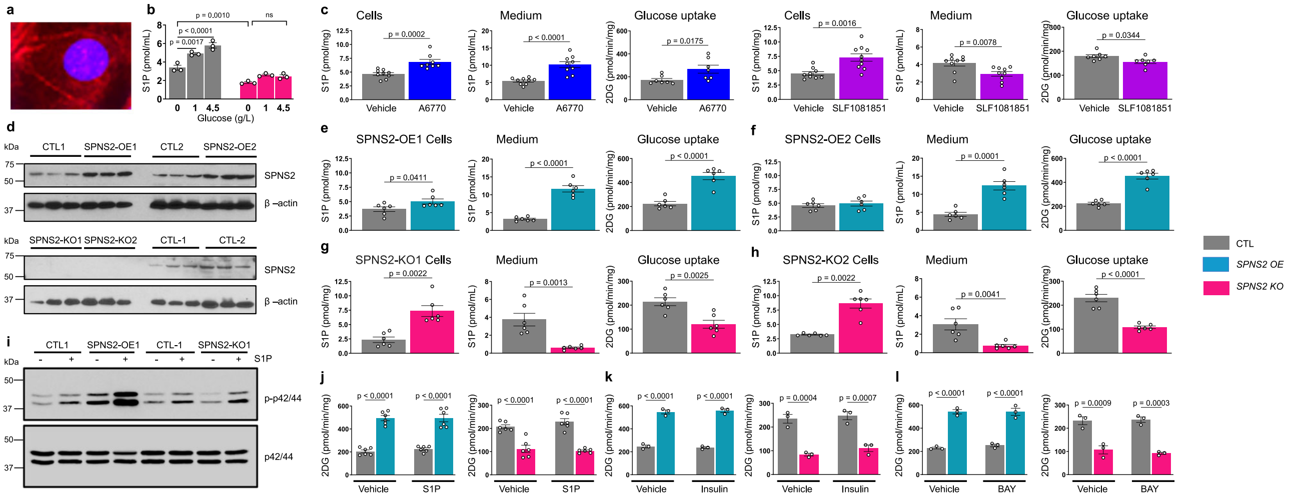

Fig. 2 | SPNS2 regulates glucose uptake. a Immunofluorescence localization of SPNS2 (red) on plasma membrane of SVEC4-10. **b** Glucose increases S1P secretion by SVEC4-10 cells (n = 3, N = 3). **c** SVEC4-10 cells were treated with S1P lyase inhibitor A6770 (200 μM) or with SPNS2 inhibitor SLF1081851 (2 μM) and levels of S1P in cells (n = 8–10, N = 5) and medium (n = 9, N = 3) as well as glucose uptake were determined (n = 7, N = 3). **d** SPNS2 expression in two SPNS2 stably overexpressing SVEC4-10 cell lines generated by CRISPR activation plasmids (CTL1, SPNS2-OE1) or lentiviral activation particles (CTL2, SPNS2-OE2) and in two SPNS2 deleted SVEC4-10 cell lines (SPNS2-KO1 generated with double nickase plasmids, and SPNS2-KO2 via CRISPR/Cas9 knock-out and homology-directed repair plasmids) compared to their controls. **e**–**h** S1P levels in cells and medium, and glucose uptake were measured in SPNS2-OE1 (**e**), SPNS2-OE2 (**f**), SPNS2-KO1 (**g**), SPNS2-KO2 (**h**). (n = 6, N = 3). **i, j** SPNS2-OE1, SPNS2-KO1 cells and their controls were treated with S1P (500 nM), and phosphorylation of p42/44 (**i**) and glucose uptake (**j**) were determined (n = 6, N = 3). **k, l** Glucose uptake in SPNS2-OE1, SPNS2-KO1 and their control cells treated with insulin (100 nM) or GLUT1 inhibitor BAY-876 (10 nM) (n = 3, N = 3). Data are means ± s.d. **b** One-way analysis of variance test followed by Šídák's multiple comparisons test. **c**–**l** two-tailed unpaired t-test. Source data are available for this figure in the Source Data file.

non-metabolized glucose tracer [^{18}F]fluoro-2-deoxy-2-D-glucose (2-FDG) after oral gavage. The distribution of 2-FDG at 60 min in WT mice was similar to that reported previously[20] as the tracer was gradually taken up into tissues and excreted into the urine. Over time, accumulation of 2-FDG in the kidneys and heart, was significantly reduced in *Spns2*$^{-/-}$ mice compared to WT, while it increased by 2.3-fold in the bladder (Fig. 1k, l). Gastric emptying, the process by which the glucose tracer leaves the stomach and moves into the intestine for absorption was similar in WT and *Spns2*$^{-/-}$ mice (Fig. 1m, o). There were also no differences in intestinal absorption (Fig. 1o), implying that SPNS2 has no significant role in glucose uptake from the intestinal lumen into the bloodstream. Notably, absorbed 2-FDG was rapidly and to a greater extent excreted into the urinary bladder of *Spns2*$^{-/-}$ mice (Fig. 1n, o), suggestive of inefficient renal reabsorption of 2-FDG from the glomerular filtrate and increased urinary excretion of glucose (Fig. 1n, o). Indeed, SPNS2 was expressed in WT kidney proximal tubules responsible for reabsorption but not in glomeruli (Supplementary Fig. 4), consistent with previous reports[9,21]. Altogether, these findings indicate that the absorption of glucose by the small intestine and its subsequent release into the bloodstream is normal in *Spns2*-deleted mice, but rather uptake of glucose from the bloodstream into tissues, as well as glucose reabsorption in the kidney are impaired, suggesting defective glucose usage or storage in the absence of SPNS2 and highlighting its potential function in glucose homeostasis.

SPNS2 overexpression increased glucose uptake and deletion reduced it

Intrigued by the apparent inverse relationship between S1P and glucose in the circulation and tissues of *Spns2*$^{-/-}$ mice (Fig. 1c–e) and acknowledging that multiple complex mechanisms regulate glucose homeostasis in mice, we were prompted to examine in more detail if and how SPNS2 can regulate glucose levels in cells. To this end, SVEC4-10 endothelial cells (EC) were selected as they represent the first physical barrier of the vascular system and express high levels of endogenous SPNS2 on the cell surface[6,10,22,23] (Fig. 2a). Increasing medium concentrations of glucose (Fig. 2b), significantly stimulated S1P secretion, suggesting that transport of S1P by SPNS2 is facilitated by extracellular glucose concentration. Next, intracellular S1P levels were increased by inhibiting the S1P-degrading enzyme, S1P lyase (SPL), with the specific inhibitor A6770[24] and the effects on glucose uptake were evaluated. As expected, inhibition of SPL not only increased intracellular S1P it also enhanced export of S1P to the medium (Fig. 2c). In addition, glucose uptake measured with its surrogate 2DG was also significantly enhanced (Fig. 2c). Furthermore, treatment of cells with the specific SPNS2 inhibitor SLF1081851[25] significantly increased intracellular S1P, decreased secretion of S1P into the medium, and notably reduced glucose uptake into the cells (Fig. 2c), hinting to the involvement of SPNS2 not only in S1P export, but also in glucose uptake.

To substantiate these findings, two independent SVEC4-10 cell lines stably overexpressing SPNS2 were generated using the CRISPR/Cas9 genome editing activation plasmid (SPNS2-OE1) or with lentiviral activation particles (SPNS2-OE2) (Fig. 2d). SPNS2-overexpressing cells significantly increased S1P export into the medium without or with minimal changes in S1P levels within the cells. Importantly, glucose uptake was also significantly enhanced in these two types of SPNS2-overexpressing cells (Fig. 2e, f). Conversely, in two SPNS2 knockout cell lines, SPNS2-KO1 (generated with double nickase plasmids) and SPNS2-KO2 (generated by CRISPR/Cas9 knock-out and homology-directed repair plasmids), S1P accumulated within the cells and S1P export and glucose uptake were significantly reduced (Fig. 2g, h). The effects on glucose uptake were confirmed by measurements of the uptake of the fluorescent 2-(N-(7-nitrobenz-2-oxa-1,3-diazol-4-yl) amino)-2-deoxyglucose (2NBD-glucose) and radiometric uptake of deoxy-D-glucose 2-[1,2-^{3}H(N)] (Supplementary Fig. 5a–c). Likewise, SPNS2 increased glucose uptake in a stably overexpressing clone (Supplementary Fig. 5b). Moreover, deletion of *Spns2* in several other cell types, including the lymphendothelial cell line SV-LEC, primary murine endothelial and epithelial cells, and lung adenocarcinoma epithelial A549 cells, significantly attenuated glucose uptake (Supplementary Fig. 5d, e). Similarly, transient knockdown of *Spns2* with siRNA also reduced glucose uptake (Supplementary Fig. 5f).

Glucose uptake and its subsequent metabolism can affect mitochondrial functions. Indeed, increased glucose uptake by overexpression of SPNS2 correlated with more ATP production (Supplementary Fig. 6a, b), enhanced basal as well as forced maximal mitochondrial respiration rates (Supplementary Fig. 6c, d), and glycolytic rates in these cells (Supplementary Fig. 6e, f), whereas SPNS2 deletion reduced all these cellular metabolic functions. Altered mitochondrial activity may reflect not only changes in glucose uptake but also, at least in part, alterations in intracellular S1P levels.

SPNS2 regulates glucose uptake independently of S1PR and GLUT1/3

It was previously reported that S1P enhances glucose uptake by transactivation of the insulin receptor by stimulation of S1P receptors (S1PR) on the cell surface[26]. In line with previous reports (reviewed in refs. 27,28), these EC express *S1pr1-3* (Supplementary Fig. 7a). Although S1P at a concentration that activates all the S1PRs[29] did not increase glucose uptake in SPNS2 knock-out or overexpressing cells, yet, it activated ERK1/2 (Fig. 2i, j). Likewise, neither treatment with S1PR agonists nor with specific S1PR1-4 antagonists affected glucose uptake in SPNS2-overexpressing cells (Supplementary Fig. 7b). Together these results indicate that SPNS2 mediates glucose uptake independently of S1P/S1PR signaling. However, a much higher concentration of S1P (10 μM) reduced glucose uptake (Supplementary Fig. 7c, d). In addition, insulin did not enhance glucose uptake in SPNS2-overexpressing or knock-out cells (Fig. 2k), consistent with the observation that dysglycemia in SPNS2 knock-out mice seems to be insulin independent (Fig. 1j and Supplementary Fig. 3e).

Next, we examined the possibility that canonical glucose transporters, including thirteen Gluts (*Glut1-13* also named *Slc2a1-13*)[30] and sodium-dependent glucose cotransporters (*Sglt1, Sglt2*), contribute to the observed increase of glucose uptake by SPNS2. Consistent with previous determinations in EC by QPCR and western blots[31–34], *Glut1* and *Glut3* were the main glucose transporters in SVEC4-10 cells with miniscule expressions of *Glut6* and *Glut10* (Supplementary Fig. 8a). *Sglt1, Sglt2*, or *Glut2,4,5,7,8,12*, and 13 were not detected, implying an absence of fructose and insulin responsive transporters. Interestingly, expression of *Spns2* was much greater than the known glucose transporters in these cells (Supplementary Fig. 8a). No changes in expression of glucose transporters were observed in SPNS2-overexpressing cells (Supplementary Fig. 8a). In agreement with previous studies[33,34], GLUT1 was localized intracellularly and only GLUT3 was on the cell surface (Supplementary Fig. 8b–e). Of note, GLUT6 and GLUT10 are also primarily localized in intracellular compartments[35]. In line with the observation that GLUT1 is cytosolic, a low concentration of BAY-876 (10 nM) that inhibits only GLUT1 did not suppress the increased glucose uptake by SPNS2 overexpression, nor did it further decrease glucose uptake in SPNS2 deleted cells (Fig. 2l). In contrast, as expected, 10 nM BAY-876 inhibited glucose uptake in stimulated T lymphocytes that express GLUT1 on the cell surface (Supplementary Fig. 8f). Importantly, a higher concentration of BAY-876 (2 μM), known to also inhibit GLUT3[31], did reduce glucose uptake in control SVEC4-10 cells, but did not affect SPNS2-mediated increase of glucose uptake in SPNS2-overexpressing cells (Supplementary Fig. 8g). Similar results were obtained with KL-11743 (Supplementary Fig. 8g), a specific GLUT1-4 inhibitor[36]. Moreover, a low concentration of maltose, known to bind to the exofacial binding sites of GLUT1 to accelerate its glucose influx[37], also had no effect on SPNS2 mediated glucose uptake or S1P export (Supplementary Fig. 8h).

It was suggested that S1P directly activates the catalytic phosphatase 2 (PP2A) subunit leading to reduction of cell surface GLUT1 and its activity in RBCs[38]. In contrast, another study reported that S1P had no effect on PP2A activity in RBCs[39]. We also found that S1P did not activate PP2A activity in vitro (Supplementary Fig. 9a). Moreover, neither the PP2A activator DT-061 nor the PP2A inhibitors, LB-100, Calyculin, or Endothall, had any significant effects on SPNS2-mediated S1P export or glucose uptake (Supplementary Fig. 9b–d). Taken together, these results suggest that SPNS2 not only mediates S1P export but also glucose uptake and metabolism independently of S1PR signaling, insulin or endothelial cell glucose transporters GLUT1 and GLUT3. Of note, SPNS2 knockout EC retained approximately 50% of their total glucose uptake capacity (Fig. 2g and Supplementary Fig. 5c, d), indicating that the remaining activity is mediated by other glucose transporters expressed in these cells, primarily GLUT1 and GLUT3. These findings are consistent with previous studies showing that GLUT1/GLUT3 knockdown in EC reduced glucose uptake by 60%[40], suggesting that the remaining 40% could be attributable to SPNS2-mediated glucose import.

Role of glucose uptake by SPNS2 in S1P-mediated functions

Certain biological processes, including cell proliferation and migration, are known to depend on SPNS2[1]. Thus, it was of interest to examine the physiological significance of coupling S1P export to glucose import. Overexpression of SPNS2 significantly increased proliferation, whereas its deletion slightly reduced it (Fig. 3a), correlating with autonomously secreted S1P levels (Fig. 2e–h). Addition of S1P to SVEC4-10 controls at a concentration that activates S1PRs (Fig. 2i) increased proliferation, yet it did not enhance proliferation of SPNS2 deleted cells (SPNS2-KO1) (Fig. 3a). Likewise, S1P enhanced the migration of control cells into the denuded gap area in a wound healing assay only in the presence of glucose; however, this effect was absent in cells lacking SPNS2 (Fig. 3b, c). Consistent with a previous selective study showing that SPNS2-driven export of S1P regulates EC barrier function[41], we found significantly decreased resistance measured by Electric Cell-Substrate Impedance Sensing (ECIS) and increased leakage of FITC-dextran through monolayers of SPNS2-KO1 compared to control cells (Fig. 3d–h). Once again, in the presence of glucose, treatment with S1P increased resistance and suppressed leakage of control cells, but not of SPNS2 deleted cells (Fig. 3f, h). Together these results suggest that SPNS2-deficient EC suffer from compromised S1P/S1PRs-mediated cellular processes due to the defective export of S1P; however, extracellular S1P concentrations that activate S1PRs cannot reverse these deficiencies probably due to lack of simultaneous SPNS2 mediated uptake of glucose.

Molecular dynamics simulations of glucose engagement by SPNS2

As the structures of hSPNS2 which shed light on its interactions with and transport of S1P have been recently resolved[14–16], atomistic molecular dynamics simulations of hSPNS2 embedded in a lipid bilayer were used to examine the possibility that SPNS2 can also import glucose. Using the inward-facing open conformation of hSPNS2 in complex with S1P in the binding site (PDB ID: 8EX4)[14] as a guide for placement of S1P, ten short, independent all-atom simulations were first performed. These simulations showed S1P exiting the binding site and moving either upward or downward, in agreement with molecular dynamics simulations of inward-facing dodecylmaltoside (DDM)-bound SPNS2 (PDB ID: 8QV6)[42]. The duration of three runs with an upward movement of the S1P headgroup was extended to 1000 ns (Supplementary movie S1). As reported previously[14], in its initial configuration, the opening formed by TMs 5, 8, and 10 of SPNS2 accommodates the polar head of S1P, and its alkyl tail take on an L shape in the midplane of the cavity (Fig. 4a and Supplementary movie S1). After a lag period, an upward movement of S1P toward the extracellular side occurred with a reorientation of its hydrocarbon chain from staggered to a vertically aligned configuration (Fig. 4a, b and Supplementary movie S1). This resulted in notable structural changes and enlargement of the extracellular vestibule of SPNS2 (Fig. 4c, d and Supplementary Fig. 10a). The Potential of Mean Force (PMF) profile shows the free-energy minima and barriers for the upward movement of S1P through

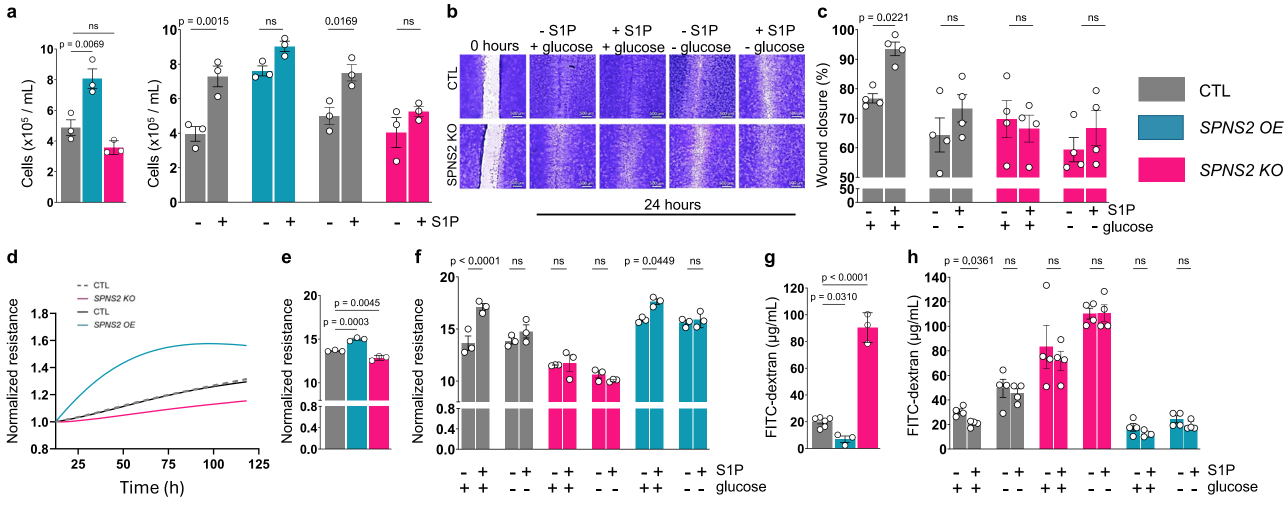

Fig. 3 | SPNS2-mediated endothelial cell functions rely on glucose uptake. **a** Proliferation of Spns2 overexpressing (SPNS2-OE1) or Spns2 deleted cells (SPNS2-KO1) and controls cells. 10^5 cells were cultured in medium containing 4.5 g/L glucose without or with 500 nM S1P as indicated and cell numbers measured after 72 h (n = 3). **b**–**f** Cells were cultured in medium without or with 4.5 g/L glucose and/or 500 nM S1P as indicated. **b**, **c** Migration of cells in wound healing assays 24 h after creating a gap in a confluent monolayer and change to media containing glucose or S1P as indicated. **b** Representative images at 0 or 24 h after initiation of migration and (**c**) percentages of wound closures determined in cell migration assays in the presence of aphidicolin (n = 4). **d**–**f** ECIS measurements of the resistance of the indicated cells. **d** Representative continuous resistance measurements. **e** normalized endpoint resistance of the indicated cells cultured for 118 h. Resistance was normalized to the value measured at 12 h. **f** Normalized endpoint resistance of the indicated cells cultured for 118 h in the absence or presence of glucose and/or S1P (n = 3). **g** FITC-dextran leakage from the indicated cell monolayers cultured in the present of glucose (n = 3, 6). **h** FITC-dextran leakage from the indicated cell monolayers in the absence or presence of glucose and/or S1P (n = 4). **a**, **c**, **e**–**h** Data are means ± s.d. ns, not significant; One-way analysis of variance test followed by Sidak's multiple comparisons test or (**h**) Welch's ANOVA multiple comparisons test. Source data are available for this figure in the Source Data file.

SPNS2 (Supplementary Fig. 10b–d). For the repositioning of S1P within the transporter, it requires overcoming an energy barrier of ~2 kcal/mol at 4.8 A to make a transition from A to B, in which S1P tail repositions by inserting further into the hydrophobic cavity. Although this is relatively modest, it is consistent with thermally accessible ligand rearrangements on biologically relevant timescales. S1P tail aligns vertically with SPNS2 after overcoming a couple of smaller barriers (Supplementary Fig. 10b–d).

Molecular docking of glucose across different PDB frames of SPNS2 obtained from the upward movement trajectory of S1P revealed that while the first few frames only allowed glucose binding on the top surface of SPNS2 (site 1) (Fig. 4e, h), the structural changes induced by S1P opened two new potential transient glucose binding pockets in the central cavity, one in the C-domain (site 2), and a second in the N-domain (site 3) close to the extracellular side (Fig. 4f, i), forming H-bonds with E433, T329, Y120, and with R119 and R200, respectively.

We next performed a molecular dynamics simulation of the SPNS2-S1P complex with docked glucose molecule in site 3 (central region of the extracellular side). The glucose initially docked on the extracellular side diffused through the central cavity, moving downward toward the intracellular side (Fig. 4g, j, l, m and Supplementary movie S2). During the extracellular to intracellular passage of glucose, it interacts with the S1P headgroup (Fig. 4k and Supplementary movie S2), suggesting that S1P may enable glucose to move through the central cavity that is now accessible (Supplementary movie S2). Of note, in the absence of S1P, molecular docking of glucose to the outward-facing conformation of hSPNS2 (PDB ID: 8EX5) followed by molecular dynamics simulation showed that all glucose molecules were transiently bound and did not traverse the central cavity or progress inward toward the intracellular side (Supplementary movie S3). Taken together, our data implies that the structural changes in SPNS2 during S1P slithering up appear to enhance glucose engagement in the inward-facing state. Notably, the most intracellular glucose binding location in the molecular dynamics simulations (site 4) overlaps with the position and pose of the modeled glucoside from dodecylmaltoside (DDM) in the experimental structures of detergent-bound SPNS2 (PDB ID: 8QV6)[42] (Supplementary Fig. 10d). The position of the DDM headgroup is restrained by the alkane chain of the detergent, preventing evaluation of glucoside binding to sites 1, 2, or 3. Nevertheless, both experimental structures and molecular dynamics simulations confirm that SPNS2 can stably coordinate glucose or glucosides at site 4.

Functional investigations of the SPNS2 glucose transport mechanism

To explore the possibility of direct binding of glucose to SPNS2 in vitro, two cell-based approaches that have been extensively used to characterize substrate binding of GLUT transporters[5,43,44] were employed. To remove interference from endogenously expressed transporters, TurboGFP-tagged hSPNS2, and TurboGFP as control were overexpressed in SVEC4-10 cells. As expected, tagged SPNS2 was localized to the cell surface (Fig. 5a). It was readily purified by affinity anti-TurboGFP nanobodies coupled to agarose beads prior to thermofluor stability assays. In addition, purified untagged hSPNS2 as well as mSPNS2-FLAG were also subjected to thermal shift assays. Changes in fluorescence intensity of 7-diethylamino-3-(4′-maleimidylphenyl)-4-methylcoumarin (CPM), a dye that is weakly fluorescent unless bound to a protein, were monitored with increasing temperature. Fluorescence increased as CPM interacted with thiols[45] or with hydrophobic patches[46] that became exposed due to thermal unfolding of purified hSPNS2 protein (Fig. 5b). Addition of glucose stabilized SPNS2 and induced a right shift with higher thermal stability. The SPNS2 apparent melting temperatures (Tm), which correspond to the inflection points of the unfolding curves, were significantly increased by addition of glucose to purified hSPNS2-TurboGFP, untagged hSPNS2, and mSPNS2-FLAG (Fig. 5c), suggesting that glucose physically binds to human and mouse SPNS2, irrespective of the tag or the purification methods.

To confirm and extend these results, scintillation proximity assays (SPA)[43] were carried out. Micelle-stabilized membrane proteins from SVEC4-10 cells overexpressing TurboGFP-tagged human or murine SPNS2, and TurboGFP and TurboGFP-tagged GLUT1 as controls, were

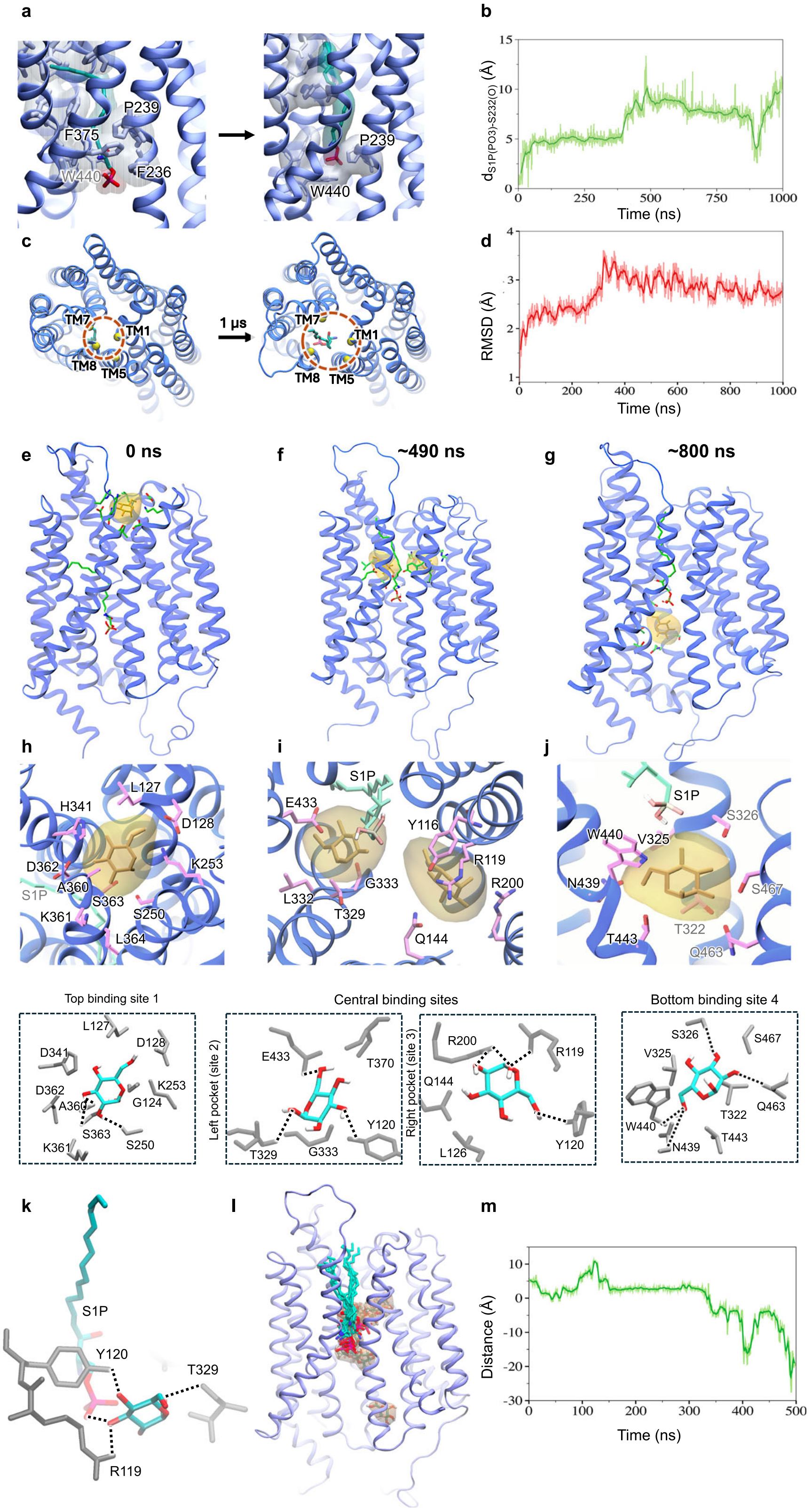

immobilized on protein A-coated scintillation beads (fluoromicrospheres) with specific anti-TurboGFP nanobody fused to rabbit IgG Fc domain allowing SPNS2 binding analysis in cell lysates. When [^{3}H]glucose binds to immobilized SPNS2 or GLUT1, the β-rays it emits are close enough to stimulate the scintillant in the fluoromicrospheres to emit light measured by a scintillation counter (Fig. 5d, e). No signal was detected with immobilized TurboGFP alone (Fig. 5e) as the energy from the unbound [^{3}H]glucose was dissipated in aqueous solution without reaching the scintillation beads. Together, these data show that glucose binds to purified SPNS2, excluding contribution from other cellular components, including endogenous transporters.

To assess the importance of the glucose binding pocket residues identified by MD simulations, E433 and T329 residues were mutated to alanine. Binding of [^{3}H]glucose to micelle-stabilized hSPNS2-TurboGFP

Fig. 4 | Molecular dynamics simulations of glucose engagement by SPNS2. **a** Molecular dynamics simulations of the inward-facing open conformation of hSPNS2 (PDB ID 8EX4) show that S1P can slither up as its hydrocarbon tail becomes vertically aligned from its kinked structure. **b** Changes in the vertical distance of the S1P phosphate headgroup from its original location near S232 of SPNS2. **c** The upward translocation of S1P causes noticeable structural changes at the extracellular vestibule of SPNS2. **d** The root-mean-squared deviation (RMSD) of the SPNS2 structure as S1P slithers upward during the unbiased simulation. The set of hydrophobic residues shown in Fig. 4a pose a barrier for the upward movement illustrated by the free-energy plot shown in Supplementary Fig. 10b–d. Once the phosphate group makes it past these residues, further upward movement is relatively easier, and the hydrophobic residues close in to obstruct its downward movement. **e**–**g** Snapshots of the representative, inward-facing open structures of SPNS2-S1P complexes at various times during the MD simulation in which S1P moves upward. Transient glucose-binding pockets were obtained by molecular docking of glucose into 2000 frames extracted from the 1000 ns simulation. **h**–**j** Close-up views of the glucose-binding pockets are shown in (**e**–**g**). Residues near the most stable glucose-binding pockets are indicated. Lower panels highlight residues within 3.5 Å of glucose in the top (site 1), central (sites 2 and 3), and bottom (site 4) glucose-binding pockets and H-bonds are indicated with dotted lines. k Glucose molecule hydrogen bonds with S1P and nearby protein residues before transitioning of glucose to the intracellular side (during 150–300 ns in the distance plot shown in **m**). **l** Trace the glucose pathway as it enters the intracellular side from the extracellular side. **m** Changes in the vertical distance of glucose from its initial position at the central site 3 binding pocket as it traverses through the channel and passes into the intracellular side. Source data are available for this figure in the Source Data file.

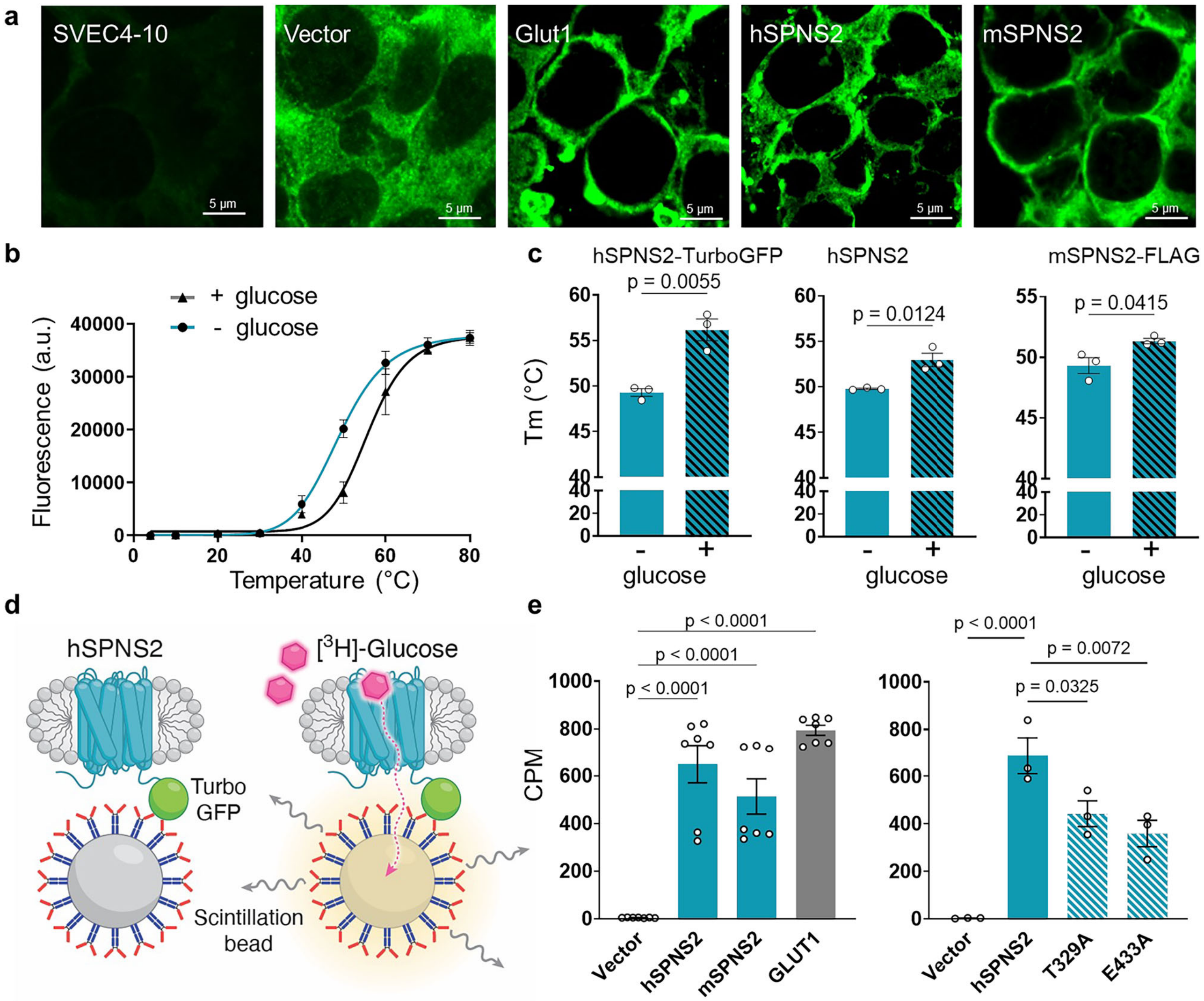

Fig. 5 | Binding of glucose to SPNS2. **a** Representative image showing localization of SPNS2-TurboGFP and GLUT1-TurboGFP. **b** Temperature shift melting curves for purified hSPNS2-TurboGFP in the absence (blue) and presence of glucose (black). (n = 3, N = 3). Values are means ± s.d. **c** Apparent melting temperatures (T_m) for hSPNS2-TurboGFP, purified untagged hSPNS2 and purified mSPNS2-FLAG were calculated from the inflection points of the fitting curves. (n = 3, N = 3). Values are means ± s.e.m. Two-tailed unpaired t-test. **d** Schematic representation of the scintillation proximity assay (SPA). TurboGFP-tagged transport proteins are bound to scintillation beads. When radiolabeled glucose binds to these bead-bound transport proteins, emitted β-rays are close enough to stimulate the scintillation beads to emit light. Illustration created by Luciana Giono. **e** SPA signals of [^{3}H] glucose (0.8 µCi) binding to TurboGFP (vector), GLUT1-TurboGFP mSPNS2-TurboGFP, and hSPNS2-TurboGFP and its mutants E433A and T329A immobilized on the surfaces of polyvinyl toluene protein A-coated scintillation beads (500 µg per well) were measured by a scintillation counter. Values are means ± s.e.m. (n = 7; N = 2) and (n = 3; N = 3). One-way analysis of variance test followed by Dunnett's multiple comparisons test. Source data are available for this figure in the Source Data file.

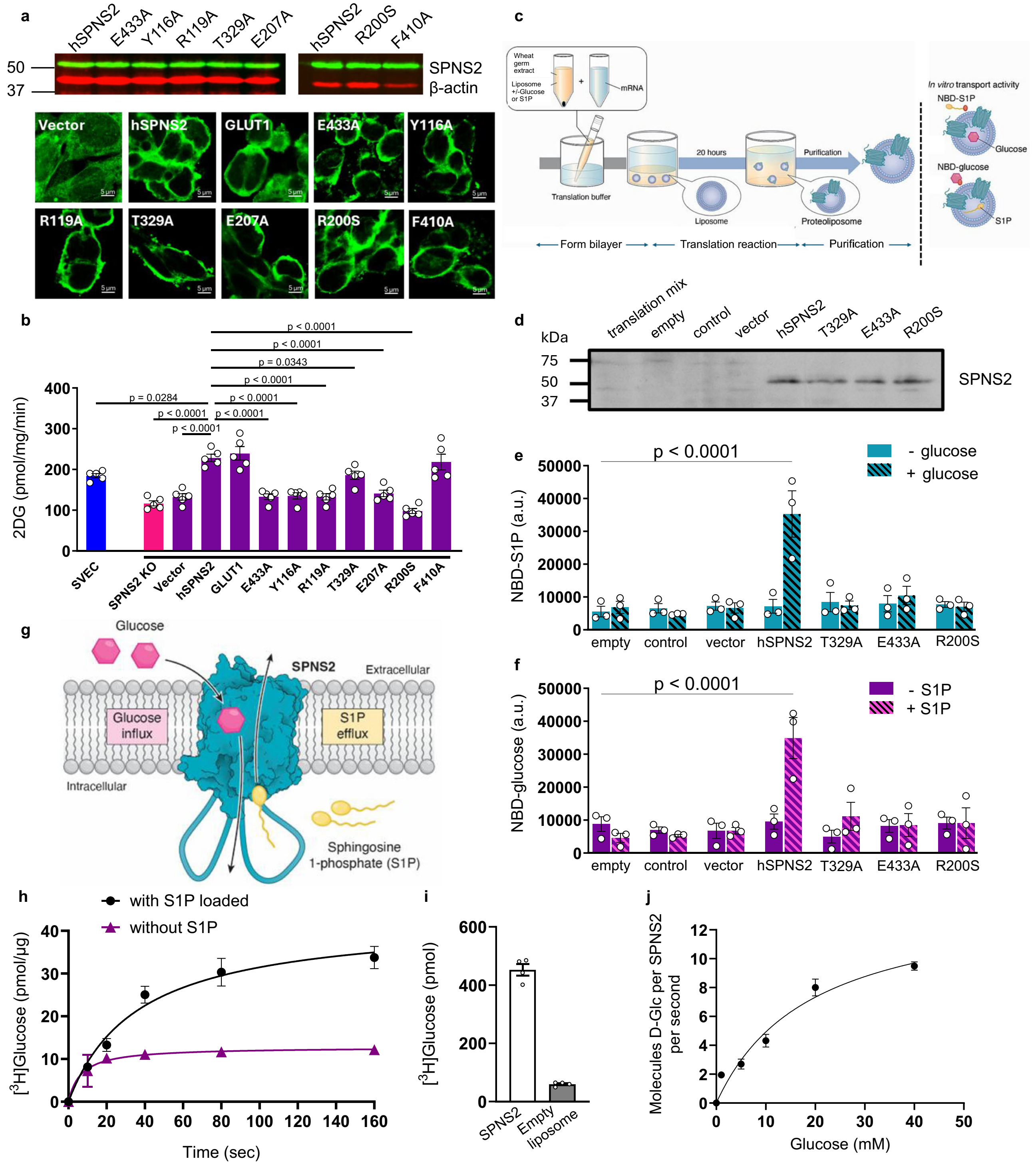

mutants E433A and T329A by SPA was substantially reduced compared to wild-type hSPNS2-TurboGFP (Fig. 5e). Lastly, complementary to binding assays, mutants of these residues were overexpressed in SPNS2-KO1 cells lacking the endogenous SPNS2 protein. All SPNS2 variants localized to the cell surface with expression levels equivalent to wild-type hSPNS2 (Fig. 6a). Of note, residues T329, R119 and R200 as well as Y116 and E207, have previously been shown to be important for S1P export[15,16,22]. As expected, overexpression of wild-type hSPNS2 or hGLUT1 in SVEC4-10 cells depleted of endogenous Spns2 increased glucose uptake (Fig. 6b). Though the E433A mutation was reported not to affect S1P export[15], but reduce it in another report[14], glucose uptake was not increased by this variant (Fig. 6b), suggesting that this residue could be important for glucose engagement. Overexpression of T329A, Y116A, and R119A mutants also do not have glucose transporter activity (Fig. 6b). Likewise, mutation of E207, which was proposed previously as an important site for the conformational change from inward-open to outward-open[47], and R200S, a known S1P transport loss-of-function mutation[22,48], also lacked glucose transport activity (Fig. 6b). In contrast, an unrelated F410A mutation at TM9 did not abrogate glucose uptake activity of hSPNS2 (Fig. 6b). Together, these results reinforce the notion that these residues within SPNS2 could also be important contacts for the transitioning of glucose from binding towards the inner cytosolic site of its central cavity in the presence of S1P.

Fig. 6 | Functional characterization of in vivo and in vitro glucose transport by SPNS2. a, **b** Identification of key SPNS2 residues involved in glucose transport. **a** Western blots and representative images of localization of hSPNS2-TurboGFP and its mutants. **b** Glucose uptake activities of SPNS2 variants with mutations in potential key residues involved in glucose or S1P engagement. hSPN*S2*, *GLUT1* vector, or the indicated mutants were overexpressed in SPNS2-KO1 cells lacking endogenous SPNS2. Glucose uptake was normalized to SPNS2 expression determined by GFP fluorescence (*n* = 5, *N* = 3). Data are means ± s.e.m. One-way analysis of variance test followed by Dunnett's multiple comparison test. **c**–**f** Direct glucose and S1P transport by SPNS2 proteoliposomes. **c** Illustration of cell-free preparation of SPNS2 proteoliposomes for functional transport analysis. **d** Comparable levels of hSPNS2 and its variants by western blots. **e**, **f** Proteoliposomes of WT hSPNS2 and variants were loaded without or with glucose (**e**) or S1P (**f**) as indicated and uptake of 1 μM NBD-S1P (**e**) or 1 μM NBD-glucose (**f**) determined. Arbitrary units (a.u.) (n = 3, N = 3). Nonspecific uptake was measured using protein-free liposomes (empty), vector containing proteoliposomes (vector), and T1R1 containing proteoliposomes (control). (n = 3, N = 3). One-way analysis of variance test followed by Dunnett's multiple comparisons test. **g** Illustration of SPNS2-mediated export of S1P out of cells while transporting glucose inward. Illustrations in panels c and g created by Luciana Giono. **h**–**j** SPNS2-mediated D-[3H]glucose uptake. **h** Time-dependent specific uptake of D-[^{3}H]glucose into hSPNS2-containing proteoliposomes that were loaded without or with S1P (n = 3–5, N = 3). Nonspecific uptake measured using protein-free liposomes (empty) was subtracted from the specific uptake. **i** Uptake of [^{3}H]glucose by hSPNS2 or empty liposomes at 40 sec (n = 4, N = 3). **j** Kinetics of D-glucose uptake by hSPNS2. Specific uptake measured at 40 sec was calculated by subtraction of nonspecific [^{3}H]glucose uptake by empty liposomes and fitted to a non-linear regression analysis using Michaelis–Menten enzyme kinetics plot with K_M, V_{max}, and k_{cat} values calculated (n = 4, N = 4). Data are means ± s.e.m. of independent experiments. Source data are available for this figure in the Source Data file.

S1P and glucose transport activities of SPNS2 in proteoliposomes

To gain better understanding of SPNS2 transporter functions, it was important to assess the in vitro transport activities of purified SPNS2 reconstituted into liposomes, a benchmark method for validation of substrate transporter pairing[5]. Recombinant SPNS2 produced by in vitro translation was directly inserted into the lipid bilayer of the liposome to form proteoliposome complexes[49] (Fig. 6c). Similar expressions of SPNS2 variants were obtained with the wheat germ cell-free protein expression system[49] (Fig. 6d). As the inside:outside ratio of protein orientation in proteoliposomes is typically even[50], we first confirmed S1P transporter activity of SPNS2 by quantifying uptake of fluorescent NBD-S1P. In glucose-loaded proteoliposomes, SPNS2 directly transported S1P compared to liposome controls, while SPNS2 proteoliposomes without glucose did not (Fig. 6e). SPNS2 transports glucose in proteoliposomes loaded with S1P but not in its absence (Fig. 6f). Similar to uptake of fluorescent NBD-glucose by SPNS2, in S1P-loaded proteoliposomes, SPNS2 directly transported [^{3}H]glucose to a much greater extent than SPNS2 proteoliposomes without S1P (Fig. 6h). Uptake by SPNS2 was saturated over seconds to minutes (Fig. 6h) and a very low level of [^{3}H]glucose accumulation was observed in protein-free liposomes (Fig. 6i). The rate of radiolabeled D-glucose uptake by SPNS2 proteoliposomes, adjusted for nonspecific uptake by empty liposomes, was assessed across varying substrate concentrations (Fig. 6J). Non-linear regression analysis estimated Michaelis–Menten constant K_m of 19.04 ± 1.34 mM and transport turnover k_{cat} of 6.88 ± 0.23 s^{-1}.

Having established in vitro proteoliposome transport assays, we then further analyzed the transport activity of SPNS2 with mutations that either have previously been reported to reduce S1P export[15,16,22,48], or were shown here to decrease glucose uptake (Fig. 6b). Notably, the SPNS2 mutants E433A, T329A, and R200S, with expression levels in proteoliposomes comparable to wild-type SPNS2 (Fig. 6d), have no significant S1P or glucose transport activities compared to vector or T1R1 containing liposome controls. In sharp contrast to these mutants, wild-type hSPNS2 greatly enhanced glucose uptake into proteoliposomes (Fig. 6e, f). Thus, SPNS2 not only exports S1P, it can also directly import glucose.

Discussion

Our study corroborated the extensive existing evidence that SPNS2 functions as a bona fide S1P transporter[1,6,7,12,14–16,22,48]. Using *Spns2* deleted mice, cells with knockdown and overexpressed SPNS2, and several complementary approaches including thermal shift and scintillation proximity assays, molecular dynamics simulations and subsequent structure-guided mutagenesis, as well as cell-free expressed SPNS2 in proteoliposome transport assays, we identified the important yet previously unrecognized feature of SPNS2 with glucose antiporter-like activity, transporting S1P out of cells and glucose in. Nevertheless, it also possible that S1P acts as an allosteric activator of glucose transit through the central region of SPNS2.

There are only a few examples of transport assays using purified mammalian GLUTs reconstituted into proteoliposomes[51,52]. Here we determined the kinetics of transport of the [^{3}H]glucose into SPNS2 proteoliposomes. The reconstituted transporter SPNS2 had similar[51] or slightly lower affinity[52] for D-glucose compared to that reported for GLUT4, the insulin-regulated glucose transporter, yet SPNS2 transported glucose with a higher turnover number than GLUT4. It is worth noting that K_m values of GLUTs for glucose in proteoliposomes are typically higher than values reported in overexpressing intact cells[35,51]. Furthermore, factors like anionic phospholipids[51] or PI(4,5)P2[17] can enhance functional transporter activity in a reconstituted-liposome system, which may influence the observed transport kinetics. As the physiological blood glucose concentration is approximately 5 mM, an intriguing possibility is that SPNS2 may fine-tune glucose uptake following a sugary meal when glucose concentrations can be very high, exceeding 20 mM.

While glucose was evidently necessary for the in vitro S1P transport by SPNS2 in proteoliposome assays, and stimulated secretion of S1P from cultured cells, S1P was still secreted even when glucose was absent from the medium. This difference might stem from variations in the duration or sensitivity of detection methods used in in vitro assays compared to those in cell culture assays that include transport activity modulators or compensatory metabolic processes. However, this data also suggests that in cells, glucose facilitates SPNS2-mediated S1P export and may not be necessary. It is also possible that SPNS2 has loosely-coupled transport mechanisms, that give rise to leak pathways which can allow SPNS2 to operate in antiport or uniport modes and could export S1P in the absence of glucose depending on conditions[53]. It is well established that enhanced phosphorylation of sphingosine, the precursor of S1P by SPHK1 increases the intracellular S1P pool that can then be exported via SPNS2[1,14,48]. Cellular levels of sphingosine exceed those of S1P by one to two orders of magnitude and can be rapidly replenished through the degradation of complex sphingolipids. In line with this, our data in cultured cells (Fig. 2c) and in mice (Supplementary Fig. 3c) show that manipulating the sphingolipid degradation pathway, which regulates cellular S1P levels modulates SPNS2-mediated glucose uptake.

Our findings raised an intriguing question of the biological functions for coupling S1P export to glucose import. It is well accepted that in response to various stimuli (growth factors, hormones, cytokines, chemokines), S1P synthesized intracellularly by activation of sphingosine kinase, is exported out of cells by SPNS2, and activates the ubiquitously expressed S1PRs on the cell surface in an autocrine or paracrine manner to regulate numerous essential physiological processes important in health and diseases[1,54]. Although erythrocyte-derived S1P is essential for developmental angiogenesis and hematopoietic-derived S1P is required for LPS-induced S1PR1 signaling during systemic inflammation[54], other biological processes such as cell growth and migration, lymphatic vascular and valve development and tissue repair, also depend on SPNS2 and S1P autocrine functions[1,28,55–57]. In addition to EC, lymphendothelial cells, epithelial and cancer cells, a variety of other cell types including pericytes, monocytes, macrophages, smooth muscle cells and microglia[58] have been reported to express *SPNS2* which is a central component of the inside-out signaling by S1P. Consistent with previous reports[9,21], we also confirmed that SPNS2 is expressed in multiple tissues, and as an example, demonstrated its distribution in the kidney. Together, these findings indicate that SPNS2 is not restricted to a specific cell type or tissue but is broadly expressed and functionally active across diverse cell populations. This broad expression supports its physiological relevance for inside-out signaling by S1P. The bidirectional coupling provides a mechanistic framework linking metabolic regulation and S1P signaling, a connection not previously established in eukaryotic transport biology. The mechanistic insight that SPNS2 couples glucose import to S1P signaling has broad implications not only to endothelial biology and glucose homeostasis, but also for the understanding of the inside-out signaling by S1P which plays a vital role in both normal physiology and disease pathology[1,59]. We have shown here that the autocrine action of inside-out signaling by S1P depends on glucose import by SPNS2. Thus, this autocrine loop uptake of glucose by SPNS2 is crucial for promoting cell growth, facilitating cell migration during wound healing, and as suggested previously[41,60], may also contribute to vascular barrier function. Simultaneous uptake of glucose is needed to provide cells with metabolic energy required for these biological processes. The additional function of SPNS2 described here may provide a mechanism to rapidly obtain glucose during S1P release and S1P/S1PR signaling so cells are bioenergetically prepared for responses to environmental stimuli. This requirement likely reflects context-specific coupling that may not be dominant in all in vivo settings, particularly where circulating or hematopoietic-derived S1P is abundant and is expected to be the primary driver of S1PR1 activation[54].

Upregulation of SPNS2 antiporter-like activity increasing S1P signaling and glucose uptake may play a role in cancer biology. The SPNS2/S1P/S1PRs axis regulates key cellular processes vital for tumor progression[1] and increased glucose uptake may provide the necessary energy and biosynthetic intermediates for rapidly dividing cancer cells. In addition, SPNS2 expression in lymphendothelial cells creates a hospitable immunosuppressive tumor microenvironment to enhance metastasis[10,61]. It is necessary to understand the elaborate relationship between SPNS2/S1P signaling and glucose absorption in different cancer types to develop effective targeted therapies. In addition, adequate glucose uptake by ECs as well as SPNS2-mediated S1P secretion help maintain endothelial barrier function[41] which prevents excessive leakage of fluids and macromolecules and regulates lymphocyte trafficking and function. Inflammation downregulates SPNS2 resulting in vascular dysfunction, permeability[41], and hypertension[62]. Coordination of glucose uptake with S1P export can thus serve as a critical mechanism for regulating vascular functions and tone, particularly under conditions of inflammation or immune activation that contribute to development of cardiovascular and metabolic diseases, as well as sepsis.

In conclusion, our study provides a link between the pleiotropic sphingolipid mediator S1P and glucose metabolism. Its significance is apparent, as glucose is the primary physiological fuel needed for energy metabolism by most cells. Abnormal SPNS2-dependent glucose uptake may explain disorders previously solely linked to SPNS2-mediated changes in S1P and subsequent S1PR signaling important for autoimmune diseases[7,12] and cancer metastases[10]. In addition, this may lead to better understanding of insulin-independent regulation of glucose uptake and potentially, involvement of SPNS2 in diabetes and other metabolic diseases.

Methods

Determination of conservation and homology

For the estimation and visualization of evolutionary conservation within the SPNS2 protein, the ConSurf web server (https://consurf.tau.ac.il/)[18] was used (run #1684017703; 05/13/2023). The human SPNS2 protein (AlphaFold monomer V2.0 prediction Q8IVW8) was submitted with the following running parameters: homologues were collected from UNIREF90 database using HMMER (19804 homologues detected) with E-value cutoff of 0.0001 and number of iterations of 1. Of these, 1370 homologues passed the thresholds (maximal overlap between homologues 10%, coverage 60%, minimal sequence identity with query sequence 35%), 1057 were CD-HIT unique (cutoff 95%). Maximal number of final homologues used for calculations was 150. The Multiple Sequence Alignments were constructed using MAFFT, and the phylogenetic tree using Neighbor Joining with ML distance. Conservation scores were determined using the Bayesian method, and the amino acid substitution model was selected based on the best fit. Pairwise Alignment Scores for the SPNS2 protein and DNA sequences with putative homologs of one another were identified with HomoloGene (https://www.ncbi.nlm.nih.gov/homologene/?term=SPNS2) and arranged according to degree of sequence identity.

Mice

The generation of Spns2tm1a(KOMP)Wtsi (referred to as tm1a/tm1a), Lyve1tm1.1(EGFP/cre)Cys/J (referred to as Lyve1cre) and Spns2tm1c(KOMP)Wtsi (referred to as tm1c/tm1c) mice have been described previously[10]. *Spns2* global knockout mice, *Spns2*$^{-/-}$ or Spns2tm1d(KOMP)Wtsi (referred to as tm1d/tm1d) were derived from germline recombination generated by crossing Spns2tm1c/tm1c mice with Cre recombinase mice resulting in globally deleted Spns2tm1d/tm1d mice. Male (wt/tm1d; Cre$^{-/-}$) were back-crossed with female (wt/tm1d; Cre$^{-/-}$). The following primer (5´to 3´) were used for genotyping: tm1d AACTTGAGAGAGGGTAGTAGGATC (498 bp), tm1c CTCATGGATGAAGGCAGGACTCAG (332 bp), wt TTCCAAGTCACAAAGCTCAATGGC (241 bp). As reported by others, the global deletion of SPNS2 led to reduced survival rates[22]. Therefore, adhering to the 3 R principles of animal welfare, the first generations of homozygous *Spns2*$^{-/-}$ and heterozygous *Spns2*$^{+/-}$ breedings were used to generate global knock-out and wild-type mice for experiments.

Global knock-out mice derived from both homozygous and heterozygous breedings with no significant differences in the measured outcomes were allocated in equal numbers together with wild-type littermates obtained from heterozygous breedings. No significant sex-based differences were observed in the measured outcomes. Mice of both sexes (aged 12–23 weeks) were used in all experiments, except for whole-body metabolic phenotyping analysis and PET scanning, which was done only in male mice due to specific experimental requirements. For individual experiments, the ages and numbers of males and females were matched to ensure consistency in the results. Glucose and S1P levels in blood and tissues were measured in the same mice. No mice were excluded from any experiment, except for one male mouse in a metabolic chamber experiment due to erroneous food intake measurements.

Mice were housed in a pathogen-free VCU vivarium under automatically controlled 12 h day-night cycles, temperature at 21–23 °C and 50–60% humidity. Mice were fed a standard diet (Teklad LM-485 Mouse/Rat Sterilizable Diet, diet 7012; Envigo, Indianapolis, IN) and water *ad libitum*. All procedures were approved by the VCU Institutional Animal Care and Use Committee protocol number AD10000996, which is accredited by the Association for Assessment and Accreditation of Laboratory Animal Care.

Whole-body metabolic phenotyping and body composition analysis

Body weights were recorded for 12-week-old male wild-type and Spns2$^{-/-}$ mice. A subset of these mice was used for body composition analysis and mice were than allocated to metabolic chamber experiments using the PhenoMaster system. Fat and lean mass were determined with the LF90II MiniSpec time-domain NMR analyzer (Bruker Optik, Massachusetts). The PhenoMaster (TSE Systems, Germany) was used to measure the metabolic phenotype in a non-invasive and continuous manner via indirect calorimetry. Mice were single-housed one week before introducing them into the individual metabolic chambers with regulated temperature (23 °C), humidity (50%), and 12 h dark/light cycles (70% light intensity). Mice were allowed to adapt for 2 days prior to measurements of VO2, VCO2, energy expenditure (EE), respiratory exchange ratio (RER), locomotor activity, food consumption, water intake, and energy balance for 7 consecutive days. Data was analyzed with the publicly available indirect calorimetry analysis tool CalR[63] (https://CalRapp.org/).

Blood and plasma analyses

Blood pH, total hemoglobin, electrolyte concentrations, and acid base status were analyzed with a ABL800 FLEX blood gas analyzer (Radiometer America Inc) directly after blood withdrawal. Plasma was collected by centrifuging blood at 2000 × *g*, 15 min, 4 °C. Plasma concentrations of triglycerides, cholesterol, non-esterified fatty acids and phospholipids were measured by the University of Cincinnati Mouse Metabolic Phenotyping Center. Fasting insulin and glucagon levels were measured by ELISA (#90080, #81518 CrystalChem).

Tissue analyses

Blood glucose levels were measured with a Nipro TRUEtrack Blood Glucose Meter (#B0727V3XQX, Amazon). Mice were euthanized by 5% isoflurane inhalation and blood was drawn by cardiac puncture with heparinized syringes. Mice were perfused transcardially with PBS with 5 U/mL heparin. Lymph was collected by cannulation of the cisterna chyli. Mouse hemoglobin A1c (HbA1c) in fresh blood was measured with the HbA1c kit (#80310, CrystalChem). Glucose levels in perfused tissues, feces, urine and lymph fluid were measured with the Glucose-Glo Assay (#J6021, Promega). 3–15 mg of tissue or feces were homogenized in 1 ml of 50 mM Tris (pH 7.5) pre-mixed with inactivation solution (0.6 N hydrochloric acid, 8:1 v/v). Tissue homogenates were neutralized with 1 M Tris base (pH 10.7) at 8:1 (v/v) and diluted 1:100–1:10,000 in buffer (50 mM Tris:0.6 N HCl:1 M Tris base at 8:1:1 ratio). For normalization, proteins were measured with the bicinchoninic acid protein assay kit (#23227, ThermoFisher). Urine and lymph fluid were diluted 1:10 – 1:1000 in PBS. For glucose quantification, diluted samples were mixed 1:1 with glucose detection reagent in white, half-area 96-well plates (#675074, Greiner bio-one), incubated for 1 h, and luminescence was recorded with the VictorX4 luminescence detector (#2030-0040, Perkin Elmer).

Glucose tolerance test

Oral glucose tolerance tests (OGTT) were carried out after 6 h fasting. Glucose (#D16-10, Thermo Scientific Chemicals) was dissolved in drinking water and administered by oral gavage (2 g/kg body weight equal to 10 μL/g body weight of a 20% glucose solution). Levels of blood glucose levels in tail vein blood were measured before and up to 120 min after gavage.

In vivo PET scanning and data analysis

PET scanning was carried out by the preclinical Bioimaging and Applied Research Core at VCU with 23-week-old WT and Spns2$^{-/-}$ mice. A MultiScan LFER 150 large bore research PET-CT (Mediso, Hungary) was used for PET and CT measurements as described[64]. Absorption and tissue distribution of orally administered glucose radiotracer [18 F]fluoro-2-deoxy-2-d-glucose (270–550 μCi) was evaluated. Following gavage, mice were anesthetized with 1% isoflurane and immediately a 1 h PET scan was initiated. For dynamic scans, the collected data were divided into 35 image frames. After completing PET data acquisition, 10 min CT scans for anatomical details were conducted. InterView FUSION software was employed for image display and tissue volume-of-interest (VOI) analysis. The initial gavaged amount was estimated from the activity detected in the whole-mouse VOI. Tracer activity in target organs was estimated by the activity in VOI of single organs at 60 min and expressed as % of whole-body activity. Gastric emptying is expressed as the difference between final and initial activities of the stomach VOI as % of whole-body activity. Intestinal absorption was calculated from the total activity in the body minus the sum of that remaining in the stomach and the intestine. Urinary excretion was calculated from the difference between initial and final activities in bladder VOI normalized to whole-body activities.

Cell culture

The mouse endothelial cell line SVEC4-10 was obtained from ATCC (#CRL-2181, Lot #70008729) and cultured in DMEM (Gibco, 4.5 g/L glucose, # 11960−044) with 10% FBS, 1 mM sodium pyruvate, and 1× GlutaMax (Gibco, #11360070, 35050061). Cells were used for up to 24 passages and tested for mycoplasma contamination using the PCR Mycoplasma Detection Kit (#G238, ABM) prior to cryopreservation. Primary endothelial and epithelial cells were isolated and cultured as described[65]. Mouse lymphendothelial cell line SV-LEC was kindly provided by Dr. J.S. Alexander (Shreveport, LA, USA) and cultured as described[66].

Generation of SPNS2 knockout and overexpressing cells

Two independent stable cell lines of SPNS2-overexpresing SVEC4-10 cells were generated by transfection of a plasmid mixture (SPNS2-OE1) and by lentiviral transduction (SPNS2-OE2) to generate a CRISPR-based synergistic activation mediator (SAM) transcription activation system, each with its own control (CTL1, CTL2). 100,000 cells in 3 ml of medium were plated in 6-well plates 24 h prior to transfection. For transfection, 125 μL of OPTI-MEM (#31985-062, Gibco) were mixed with 10 μL Lipofectamine 3000 Reagent (#100022050, Invitrogen). Separately, 125 μL of OPTI-MEM were mixed with 10 μL P3000 Reagent (#100022057, Invitrogen), and 2 μg murine SPNS2 CRISPR Activation Plasmid mixture (#sc-432145-ACT, Santa Cruz Biotechnology) generating a synergistic activation mediator (SAM) transcription activation system for the upregulation of gene expression. The mixture contained three plasmids in a 1:1:1 mass ratio (1 plasmid encoding deactivated Cas9 nuclease (D10A and N863A) fused to the transactivation domain VP64, and a blasticidin resistance gene; 1 plasmid encoding the MS2-p65-HSF1 fusion protein, and a hygromycin resistance gene; 1 plasmid encoding a *Spns2*-specific 20 nt guide RNA (gRNA) fused to two MS2 RNA aptamers, and a puromycin-resistance gene). For the generation of control cells, 2 μg Control CRISPR Activation Plasmid mixture (#sc-437275, Santa Cruz Biotechnology) was used. Diluted DNA was mixed with the transfection reagent and incubated for 15 min. Prior to transfection, the cell culture media was replaced with fresh media and the DNA-lipid-mixture was added dropwise. 48 h post-transfection, the media was replaced with culture media containing 2 μg/mL puromycin dihydrochloride, 300 μg/mL hygromycin B and 5 μg/mL blasticidin-S-HCl (#sc-108071, #sc-29067, #sc-495389, Santa Cruz Biotechnology). For the transduction of lentiviral particles, cells were seeded as described above. Prior to transduction, the media was replaced with complete media containing 5 μg/mL Polybrene (#TR-1003-G, Sigma-Aldrich). Cells were transduced by adding thawed and mixed SPNS2 Lentiviral Activation Particles (#sc-432145-LAC, Santa Cruz Biotechnology) or Control Lentiviral Activation Particles (#sc-437282, Santa Cruz Biotechnology) containing SAM and were selected 24 h post-transduction as described above.

Two SPNS2-knockout SVEC4-10 cell lines were generated: SPNS2-KO1 by transfection of a double nick of the genomic SPNS2 DNA mimicking a double-strand break that is repaired by error-prone nonhomologous end joining; and SPNS2-KO2 by transfection of SPNS2 CRISPR/Cas9 KO and SPNS2 homology-directed DNA repair (HDR) plasmids, using SPNS2 Double Nickase Plasmids (#sc-432145-NIC, Santa Cruz Biotechnology) or SPNS2 CRISPR/Cas9 KO Plasmids (#sc-432145, Santa Cruz Biotechnology), respectively. Briefly, the SPNS2 Double Nickase Plasmid mixture contains a pair of plasmids each encoding a D10A mutated Cas9 nuclease and a target-specific 20 nt gRNA. One pair encodes a puromycin-resistance gene. Paired gRNA sequences are offset by about 20 nt for double nicking of the genomic DNA. Control Double Nickase Plasmids (#sc-437281, Santa Cruz Biotechnology) were used to generate control cells. SPNS2 CRISPR/Cas9 KO Plasmids consist of a pool of three plasmids each encoding the Cas9 nuclease and a Spns2-specific 20 nt gRNA and were co-transfected with SPNS2 HDR Plasmids (# sc-432145-HDR, Santa Cruz Biotechnology) containing 2–3 plasmids with HDR templates corresponding to the cut sites generated by the SPNS2 CRISPR/Cas9 KO Plasmid. Control CRISPR/Cas9 Plasmids (#sc-418922, Santa Cruz Biotechnology) were used to generate control cells. Transfections were carried out as described above, while SPNS2 CRISPR/Cas9 KO Plasmids were transfected in the presence of 5 μM L-755,507 (#sc-204045, Santa Cruz Biotechnology). 48 h post-transfection, media was replaced by culture media containing 2 μg/mL puromycin dihydrochloride. Cells were selected for 4 weeks, and media was replaced by regular culture medium at least 1 week prior to experiments.

In vitro cell treatments

Cells were seeded (200,000 cells/6-well) and 24 h later, the cell culture medium was replaced with glucose-free DMEM (Gibco, # A14430-01, phenol-red and glucose-free) with 10% FBS, 1 mM sodium pyruvate, and 1× GlutaMax for 4 h. The medium was then replaced by DMEM without or with 1 g/L or 4.5 g/L glucose (#G8644, Sigma) for 24 h. In other experiments, cells were treated with 200 μM of the S1P lyase inhibitor A6770 (#29972, Cayman Chemical Company), 2 μM of the SPNS2 inhibitor SLF1081851 (#HY-149004, MedChemExpress), or the corresponding vehicles in medium with 4.5 g/L glucose for 24 h. Where indicated, cells were treated with 500 nM or 10 μM S1P (#860492, Avanti Polar Lipids) for 30 min, 100 nM insulin (#C-52310, PromoCell) for 4 h, 10 nM BAY-876 (#HY-100017, MedChemExpress) for 4 h, or with 1 μM LB-100 (#HY-18597, MedChemExpress), 10 μM DT-061 (#HY-112929, MedChemExpress), 2 nM Calyculin A (#HY-18983, MedChemExpress), or 100 nM Endothall (#HY-113976A, MedChemExpress) for 24 h in medium with 4.5 g/L glucose.

Analysis of S1P

10–50 μL of blood or plasma in 2 ml methanol was used for the determination of S1P. Weighed tissue samples were placed into 13 × 100 mm borosilicate tubes and homogenized in 2 ml methanol. Cell culture medium was mixed with methanol 1:1 (v/v) and dried with a speed vac and resuspended in 2 ml methanol. Internal standard (Avanti Polar Lipids, Alabaster, AL) in 10 μL ethanol:methanol:water (7:2:1) as a cocktail of 250 pmol each were added to samples. Standards for sphingoid bases and sphingoid base 1-phosphates were 17-carbon chain-length analogs. Samples were dispersed by sonication at room temperature for 30 s. 1 mL of chloroform was added to achieve methanol:chloroform at 2:1. The mixtures were incubated at 48 °C for 8 h. The extracts were centrifuged and the supernatants transferred to new tubes, dried with a speed vac and reconstituted in 0.5 mL of the starting mobile phase solvent for LC-ESI- MS/MS analysis, sonicated and centrifuged, and supernatants transferred to autoinjector vials. Sphingolipids were separated by reverse-phase HPLC using a Supelco 2.1 × 50 mm Ascentis Express C18 column (Sigma) with a binary solvent system at a flow rate of 0.5 mL/min with a column oven set at 60 °C. Prior to injection of samples, the column was equilibrated for 0.5 min with a solvent mixture of 95% mobile phase A1 ($CH_3OH/H_2O/HCOOH$, 58/41/1, v/v/v, with 5 mM ammonium formate) and 5% mobile phase B1 ($CH_3OH/HCOOH$, 99/1, v/v, with 5 mM ammonium formate), and after sample injection, the A1/B1 ratio was maintained at 95/5 for 2.25 min, followed by a linear gradient to 100% B1 over 1.5 min, which was held at 100% B1 for 5.5 min, followed by a 0.5 min gradient return to 95/5, v/v, A1/B1. The column was re-equilibrated with 95:5, v/v, A1/B1 for 0.5 min before each run. The HPLC column was coupled to a Sciex 5500 quadrupole/linear ion trap (QTrap; SCIEX Framingham, MA) operating in triple quadrupole mode. Q1 and Q3 were set to pass molecularly distinctive precursor and product ions (or a scan across multiple m/z in Q1 or Q3), using N_2 to collisionally induce dissociations in Q2 (which was offset from Q1 by 30–120 eV). The temperature of the ion source was set at 300 °C. Data was collected using multiple reaction monitoring (MRM) and positive ionization $[M + H]^+$ was used for qualitative analysis and quantification. The following MRM transitions were used for quantification: m/z = 380 → 264 for S1P and m/z = 366 → 250 for d17:1 S1P. Analyst 1.6 software was used for data acquisition and analysis.

Glucose uptake by cells

Glucose uptake into cells was measured with the Glucose Uptake-Glo Assay (#J1342, Promega). Cells were seeded and treated as described above and washed three times with PBS. Cells were then incubated with 1 ml of 1 mM 2-deoxyglucose for 10 min. 500 μL stop buffer was added and 75 μL transferred to white opaque 96-well plates (#15042, Thermo Scientific) and 25 μL neutralization solution added. After incubation with 100 μL of detection reagent for 1 h, luminescence was recorded with the VictorX4 luminescence detector.

[^{3}H]Deoxyglucose and 2NBD-glucose uptake

Cells were washed with Krebs-HEPES solution (NaCl 113 mM, KCl 3 mM, KH2PO4 1.2 mM, MgSO4 1.2 mM, CaCl2 2.5 mM, NaHCO3 25 mM, glucose 5.5 mM, HEPES 1.5 mM, pH 7.2) and incubated with 16.7 nM deoxy-D-glucose [1,2-3H(N)] (5.4 Ci/mmol, #TRK672, Amersham) for 60 min, washed 3 times with PBS, and then lysed in 0.3 M NaOH. Radioactivity in the lysates was measured with a Beckman Coulter LS6500 Scintillation Counter and the data normalized to total cellular proteins. In some experiments, cells were starved for 4 h in glucose-free medium, treated for 10 min with 200 μg/ml of 2NBD-glucose, 2-deoxy-2-[(7-nitro-2,1,3-benzoxadiazol-4-yl)amino]-D-glucose (#11046, Cayman Chemical Company), a fluorescently-labeled deoxy-glucose analog, washed and fluorescent signals were recorded by microplate reader at excitation/emission wavelengths 485/535 nm.

Western blotting

Cells were lysed in RIPA buffer (150 mM sodium chloride, 1% Nonidet P-40, 0.5% sodium deoxycholate, 0.1% sodium dodecyl sulfate, 25 mM Tris pH 7.4), and Halt protease and phosphatase inhibitor cocktail (#1861281, Thermo Scientific). After adding denaturating Laemmli buffer, samples were heated for 30 min at 56 °C. Proteins were separated on 12% SDS-PAGE gels and transferred to nitrocellulose membranes (0.2 μm pore size). Membranes were blocked for 1 h in 5% milk in TBS-T (#1706404 BioRad), incubated overnight at 4 °C with primary antibodies (α-SPNS2, #ab59972, Abcam; #SPNS2-101AP, FabGennix, α-β-actin, #3700S, Cell Signaling; α-p-p42/44, #4377S, Cell Signaling; α-p42/44, #4695S, Cell Signaling) at 1:1,000 dilutions in 5% milk in TBS-T, washed, and subsequently incubated with secondary antibodies (diluted 1:5000 in 5% milk) for 2 h at room temperature. After washing, immunopositive bands were visualized by enhanced chemiluminescence with Azure 600 imaging system or x-ray film developer.

RNA isolation and quantitative polymerase chain reaction

Total RNA from cultured mammalian cells was isolated with the Monarch Total RNA Miniprep Kit (#T2010S, New England Biolabs) with on-column DNase 1 treatment. Quality and concentration of isolated RNA was determined with the NanoDrop (Peqlab). The High-Capacity cDNA Reverse Transcription Kit (#4368813, Applied Biosystems) was used for cDNA synthesis. To determine mRNA levels, cDNA (100 ng) was amplified using specific pre-designed primers (KiCqStart SYBR Green Primers KSPQ12012G; Primer pair IDs: M_Actb_1, M_Hprt_1, M_Polr2a_1, M_Tbp_1, M_B2m_1, M_Slc2a1_1, M_Slc2a2_1, M_Slc2a3_1, M_Slc2a4_1, M_Slc2a5_1, M_Slc2a6_1, M_Slc2a7_1, M_Slc2a8_1, M_Slc2a9_1, M_Slc2a10_1, M_Slc2a12_1, M_Slc2a13_1, M_Slc5a1_1, M_Slc5a2_1, M_Slc5a3_1) and for Spns2 the following primer pair (5′-3′): forward CTCATCTTTGGAGCCATTAC and reverse AAAATGCAGATATAAGCGCC with the Power SYBR Green PCR Master Mix (#4367659, Applied Biosystems). Analysis was performed with a CFX Opus 96 Real-Time PCR Detection System (#12011319, BioRad). To evaluate the optimal reference gene five reference genes (beta-actin (Actb), hypoxanthine phosphoribosyltransferase 1 (Hprt), RNA polymerase II subunit A (Polr2a), TATA box binding protein (Tbp), beta2-microglobulin (B2m) were analyzed across all samples and ranked according to their expression stability with the NormFinder algorithm as described[67]. Hprt and Polr2a were identified as the best combination. Target mRNA expression levels were evaluated using the change-in-threshold (Ct) values normalized by the mean Ct value of Hprt and Polr2a per sample. Relative changes in gene expression were determined by the 2(-Delta Delta C(T)) method with the relative expression software tool (REST) based on mathematical model and a pairwise fixed reallocation randomization test[68].

Cell surface expression of glucose transporter 1 (Glut1)

Single cell suspensions of Spns2 overexpressing or knock-out cells were centrifuged (300 × *g*, 10 min) and washed with flow buffer (PBS with 2 mM EDTA and 0.5% BSA). After centrifugation, the cell pellet was resuspended in flow buffer and two vials per sample each with 105 cells were aliquoted. One Aliquot was stained with 5 μg anti-GLUT1 (extracellular)-FITC (#AGT-041-F, Alomone Labs), the other with 5 μg rabbit IgG Isotype Control-FITC (#RIC-001-F, Alomone Labs) for 30 min at room temperature. After washing, cells were then fixed with FluoroFix Buffer (#422101, BioLegend). Cells were washed and resuspended in flow buffer for analysis with a BD LSRFortessa X-20 Cell Analyzer (BD Bioscience) equipped with BD FACSDiva 8.0 software for acquisition. As a positive control, primary T lymphocytes from WT animals were isolated from the spleen with a combination of CD4 (L3T4) and CD8a (Ly-2) MicroBeads (#130-117-043, 130-117-044, Miltenyi Biotec) and magnetic-activated cell sorting. Isolated T lymphocytes were left untreated or stimulated with surface-coated monoclonal anti-CD3ε (5 μg/mL diluted in PBS, incubated for 2 h at 37 °C for immobilization; #100301, BioLegend) and 1.7 μg/mL monoclonal soluble anti-CD28 (#102101, BioLegend) for 24 h as described[69]. Cells were then stained and analyzed as described above. Data analysis was performed with FlowJo version 10.8.1 (BD Life Sciences).

Cell metabolic analysis

ATP production rates, mitochondrial respiration, and glycolytic rates were assessed with the Seahorse XF Real-Time ATP Rate Assay Kit (#103592-100, Agilent Technologies), the Seahorse XF Cell Mito Stress Test Kit (#103015-100, Agilent Technologies), and the Seahorse XF Glycolytic Rate Assay Kit (#103344-100, Agilent Technologies) with the Seahorse XFe24 Analyzer (Agilent Technologies). Data was normalized to the protein content per well (determined by BCA Protein Assay Kit) and analyzed with the report generators provided by Agilent Technologies.

Immunohistochemistry

Paraformaldehyde-fixed organs were processed, stained and imaged by the Tissue and Data Acquisition and Analysis Core (TDAAC) at VCU. For blocking peptide experiments, the primary SPNS2 antibody (#MBS5400801, MYBioSource) was diluted 1:100 in PBS with 1% BSA and incubated with a 5-fold excess of blocking peptide (#MBS5400654, MYBioSource) or buffer for 30 minutes at RT. Processed tissue slides were then incubated with primary antibody or blocked antibody according to standardized procedures.

Cell migration assays

Endothelial cell migration was assessed with the CytoSelec 24-Well Wound Healing Assay (#CBA-120, CellBiolabs). Briefly, cells were seeded in 24-well plates with an insert creating a wound field with a defined gap and cultured in complete medium until confluent. To initiate the assay, the insert was removed. Detached cells were removed by gently washing with PBS. Cells were then cultured in medium without or with glucose (4.5 g/L) and/or S1P (500 nM) and incubated at 37 °C with 5% CO_2 for the duration of the assay in the presence of aphidicolin (5 ug/mL, # BML-CC101-0001, Enzo Life Sciences) to inhibit cell proliferation. As control, one well was incubated with the insert till completion. After 24 h, the media was removed, and the cells were stained with cell staining solution, washed three times with deionized water and images of the wound areas were captured and quantified with Image J software.

Electric cell-substrate impedance sensing (ECIS)

ECIS arrays (96W10idf PET plates, Applied Biophysics) were coated with 0.2% gelatin (200 μL, Sigma-Aldrich). Cells were seeded at a density of 0.2×10^5 cells/well to achieve confluence shortly after the start of culture. After 12 h, the medium was replaced with medium without or with glucose (4.5 g/L) and/or S1P (500 nM). Resistance was recorded at low frequencies (4000 Hz) for 5 days with Z-Theta (Applied BioPhysics) and analyzed with Applied BioPhysics – ECIS Software v1.2.186.0 PC.

Dextran permeability assay

Cells were seeded onto transparent polyethylene transwell inserts (0.4 μm pores, Sarstedt) in 24-well plates with 600 μL and 200 μL medium in the lower and upper chambers, respectively, and grown to confluency. Then the medium in the upper and lower chambers was replaced with medium without or with glucose (4.5 g/L) and/or S1P (500 nM) and the upper chamber also contained 2 mg/mL 70 kDa FITC-dextran (Sigma-Aldrich). FITC-dextran permeability into the lower chamber was measured after 24 h of incubation at 37 °C with 5% CO_2 using an Infinite 200 plate reader (Tecan) at 485 nm excitation and 530 nm emission.

PP2A activity

PP2A was measured with the PP2A Immunoprecipitation Phosphatase Assay Kit (#17-313, Merck Millipore). Cells treated as described in figure legends were lysed in 200 µl cold buffer containing 20 mM imidazole-HCl, 2 mM EDTA, 2 mM EGTA (pH 7.0) with 10 µg/mL each of aprotinin, leupeptin, antipain, soybean trypsin inhibitor, 1 mM benzamidine, and 1 mM PMSF. Lysates are then incubated for 2 h at 4 °C with 4 µg of anti-PP2A catalytic subunit antibody (clone 1D6, # 05-421) and 40 µL Protein A agarose slurry (Catalog # 16-125). Beads were washed 3 times with TBS (200 mM Tris, 1500 mM NaCl, pH 7.4) and one time with Ser/Thr Assay Buffer. Afterward, 60 µL of phosphopeptide (750 μM) were added and incubated for 10 min at 30 °C. 25 µL of the mixture was transferred to half-well plates and mixed with 100 µL Malachite Green phosphate detection solution. The activity of PP2A was assessed by dephosphorylation of the phosphopeptide (K-R-pT-I-R-R) detected the green complex formed between Malachite Green, molybdate, and free orthophosphate measured at 650 nm in a plate reader after 15 min. In some experiments 0.58 mU of human recombinant PP2A catalytic subunit (#10011237, Cayman Chemical) in 100 µL was incubated with S1P (1 μM), LB-100 (1 μM) or Calyculin A (2 nM) for 10 min and PP2A activity determined.

Molecular modeling and simulations

The inward-facing open structure of hSPNS2 with S1P was obtained from the RCSB protein data bank, PDB ID: 8EX4. This recently solved cryoEM structure[14] has the S1P tail wedged deeper into a cavity and its phosphate headgroup pointing toward the cellular side. Residues 99 to 539 were considered for the simulations. Systems with or without glucose and S1P were prepared for molecular dynamics simulations. Ten independent 200 ns simulations were performed for the hSPNS2-S1P complex without glucose for the inward-facing open structure. Several simulations showed S1P leaving the binding site and moving downward closer to the intercellular side suggesting that S1P can move to and from its binding site. For the run showing slight upward movement of the S1P headgroup, the simulation was extended to 1000 ns and two additional replica runs were performed. To obtain glucose-bound complexes, 2000 frames were extracted from one of the 1000-ns simulations, and molecular docking of glucose was performed on these frames using AutoDock Vina[70] and AutoDockTools[71]. The SPNS2-S1P complex with glucose molecules docked to the extracellular side was simulated for 600 ns. Two additional replica runs were performed for 1000 ns each. For simulating hSPNS2 with glucose but without S1P, molecular docking of glucose was performed on the outward-facing SPNS2 structure, PDB ID 8EX5 (three replicas 600 ns each).

For molecular simulations, the membrane-embedded hSPNS2 systems were prepared with the membrane builder interface of CHARMM-GUI[72,73]. An asymmetric lipid bilayer[74,75] was generated using the lipids POPC:POPE:PSM:POPS:PIP2:CHOL in the ratio of 41:8:23:4:4:20 in the upper leaflet and 11:37:5:16:10:21 in the lower leaflet (Supplementary Table 1), representing the complex lipid composition of the human plasma membrane[74]. The systems were solvated in TIP3P water model[76] and ionized and neutralized with a 150 mM concentration of K^+ and Cl^- ions. Brief information on the final systems is given in Supplementary Table 2. Each system was minimized for 10,000 steps, followed by a 1125 ps equilibration using the six-step equilibration protocol of CHARMM-GUI. The temperature and pressure were controlled during the simulations using Langevin temperature coupling (with 1 ps−1 friction coefficient)[77] and Nose–Hoover Langevin-piston method (piston period 50 fs, decay period 25 fs)[78]. Covalent bonds involving hydrogen atoms were fixed using the SHAKE algorithm[79]. The nonbonded cutoff was set to 12 Å, and the long-range ionic interactions were treated with the particle mesh Ewald method[80,81]. Molecular dynamics simulations were performed using the GPU-enabled NMAD 3.0 software[82].

Potential of mean force (PMF) calculation

The Potential of Mean Force (PMF) for SPNS2::S1P system was calculated using weighted histogram analysis method (WHAM) with umbrella sampling[83]. A total of 23 windows were created along the reaction coordinate (the center of mass distance between O3 of S1P and the backbone O of S232). The system for each window was minimized and equilibrated, followed by a 20-ns NPT (constant number, pressure, temperature) production simulation using the collective variable (colvar) module in NAMD with a harmonic force constant of 2.5 kcal/mol. System preparation, visualization, and analysis were used with VMD[84] and PyMOL (https://www.pymol.org/).

Generation of TurboGFP-tagged Spns2 overexpressing cells and site-directed mutagenesis

To overexpress TurboGFP-tagged SPNS2 for ligand binding studies, SVEC4-10 cells were transfected with 2 μg of SPNS2 (NM_001124758) Human Tagged ORF Clone in pCMV6-AC-GFP (#RG225940, Origene), 2 μg of Spns2 (NM_153060) Mouse Tagged ORF Clone in pCMV6-AC-GFP (#MG218672, Origene), or as controls with 2 μg of the pCMV6-AC-GFP vector (#PS100010, Origene) or 2 μg of glucose transporter GLUT1 (SLC2A1) (NM_006516), or Human Tagged ORF Clone in pCMV6-AC-GFP (#RG222696, Origene). 24 h post-transfection, stable expressing cells were selected for at least 4 weeks with 400 μg/mL G418 (#NC9107150, Invivogene), and media was replaced by regular culture medium at least 1 week prior to experiments.

For cell lines overexpressing single amino acid exchanged mutant variants of the human SPNS2, SVEC4-10 cells with a knock-out of endogenous Spns2 created by double nickase plasmids (SPNS2-KO1) were used. Amino acid exchange by site-specific mutagenesis, e.g. substitution of single nucleotides, was performed with the Q5 Site-Directed Mutagenesis Kit (#E0554S, New England Biolabs) and double-stranded SPNS2 (NM_001124758) Human Tagged ORF Clone in pCMV6-AC-GFP. Mutagenic primers were designed with www.NEBaseChanger.neb.com. Sequences and corresponding melting (Tm) and resulting recommended annealing temperatures (Ta) for each reaction are listed in Supplementary Table 3. After whole-plasmid-sequencing, successful mutated plasmids, the unmodified SPNS2 (NM_001124758) Human Tagged ORF Clone in pCMV6-AC-GFP, or as controls pCMV6-AC-GFP vector or Glucose Transporter GLUT1 (SLC2A1) (NM_006516) Human Tagged ORF Clone in pCMV6-AC-GFP were transfected in SVEC4-10 knockout cells, SPNS2-KO1. Stable expressing cells were selected as described above with 400 μg/mL G418. Expression level and localization of SPNS2 in the mutants was verified by GFP fluorescence quantitation.

Fluorescent thermal stability assay

SVEC4-10 cells overexpressing TurboGFP-tagged SPNS2, TurboGFP-tagged GLUT1 or TurboGFP were cultured and lysed in Pierce GPCR Extraction and Stabilization Reagent (#A43436, Thermo Scientific), preserving and stabilizing the native protein structure in a detergent micelle. For protein purification, lysates were mixed with anti-TurboGFP nanobody (VHH) covalently bound to agarose beads (#tbtak-20, ChromoTek) and incubated for 4 h at 4 °C. After elution under non-denaturing conditions, the amount of purified protein was determined by BCA assay. 10 μg purified protein was diluted in 0.5 mL dilution buffer (20 mM HEPES (pH 7.5), 200 mM NaCl, 0.025% N-dodecyl-β-d-maltoside (DDM; #D310, Anatrace), and Halt protease and phosphatase inhibitor cocktail. After 5 min equilibration at room temperature, 250 μL of each sample was incubated with 25 μL D-glucose (10 g/L, #G8644, Sigma) or water as vehicle for 30 min at 4 °C. 7-diethylamino-3-(4′-maleimidylphenyl)-4-methylcoumarin (CPM dye; #D346, Invitrogen) was diluted 1:40 in dilution buffer and 20 μL of diluted CPM dye was added to glucose or vehicle containing samples (final 0.1 mg protein/mL). 25 μL aliquots were heated in 0.2 mL PCR tubes with a ramp rate of 2 °C/min in a T100 PCR thermal cycler (BioRad). 20 μL of samples from 4 °C or heated to 80 °C were transferred to black 384-well plates (#7811209, Greiner Bio-One) and fluorescence measured (excitation of 387, emission at 463 nm) with a TECAN Infinite M1000. Protein unfolding was determined as increase in CPM fluorescence intensity with increasing temperature as described[45]. Increased melting temperature indicated increased thermostability due to ligand binding. Purified untagged hSPNS2 or murine FLAG-tagged SPNS2 were analyzed similarly. Purification of untagged hSPNS2 was described previously[17,85]. Murine FLAG-tagged SPNS2 was purified from HCT116 cells overexpressing FLAG-tagged mouse Spns2 coding pCMV6- Entry plasmid (#MR218672, Origene). Cells were lysed as described above and immunoprecipitated with anti-FLAG antibody conjugated magnetic beads (#A36797, ThermoFisher). Immunoprecipitates were washed extensively with lysis buffer, and FLAG-SPNS2 was eluted from the beads by incubation in lysis buffer containing 2 mg/mL FLAG peptide (#RP10586, GenScript) for 1 h at 4 °C.

Scintillation proximity assay

Binding of glucose to SPNS2 or GLUT1 was measured by scintillation proximity assays (SPA) as described[43] with some modifications. Lysates of SVEC4-10 cells overexpressing TurboGFP-tagged SPNS2 and its

T329A and E433A mutants, TurboGFP-tagged GLUT1 or TurboGFP were prepared as described above. 100 µL SPA buffer (50 mM Tris-HCl (pH 8), 150 mM NaCl, 20% glycerol and 0.08% DDM), 0.8 µCi Glucose D-[5-3H(N)] (#NET531005MC, Perkin Elmer), 20 µg total cell lysate, and 100 ng recombinant anti-TurboGFP nanobody VHH-rabbit IgG Fc fusion (#tbfrb-100, ChromoTek) were added to each well of 96-well white Perkin Elmer LLC Isoplates (#6005040, Perkin Elmer) and incubated at room temperature for 5–30 min. Subsequently, 0.5 mg polyvinyl toluene (PVT) protein A SPA beads, called fluoromicrospheres (#RPNQ0019, Perkin Elmer) in 50 µL SPA buffer were added to each well. Plates were sealed and reaction mixtures were incubated for 8 h at 4 °C with mild agitation. When 3H-labeled glucose binds to the SPA bead-bound SPNS2, their emitted β-rays are close enough to stimulate the fluoromicrospheres to emit light, which is measured by a MicroBeta2 plate counter (Perkin Elmer). Specific counts were determined by subtracting a reaction containing only lysis buffer.

SPNS2 localization

SVEC4-10 cells or cells overexpressing TurboGFP-tagged SPNS2 were cultured on coverslips in 24-well plates and fixed with 3.7% formaldehyde. After blocking with PBS containing 5% normal goat serum, 1% BSA, and 0.04% Triton X-100 for 1 h, slides were incubated with rabbit anti-SPNS2 (#ab82629, 1:100, Abcam) or with mouse monoclonal anti-TurboGFP (#TA150041, 1:200, Origene) for 1 h. Slides were washed followed by incubation with secondary anti-rabbit conjugated with Alexa Fluor 555 (#A21428 1:200, Invitrogen) or goat anti-mouse antibody conjugated with Alexa Fluor 488 (#A11001, 1:200, Invitrogen) for 1 h. Nuclei were stained with DAPI (Invitrogen) and cells imaged with a Zeiss LSM confocal microscope equipped with a Becker & Hickl Fluorescence Lifetime Imaging system.

Preparation of SPNS2 proteoliposomes

The Proteoliposome PLUS Expression Kit (# CFS-EDX-PLUS-PLE, Cell-Free Science) and the pEU-E01-MCS expression vector for wheat germ cell-free protein expression system were used as described with some modifications[86]. In the presence of extracts from soybean azolectin (containing 25% phosphatidylcholine, 25% phosphatidylethanolamine, 25% phosphatidylinositol, and small amounts of other phospholipids from soybeans) in the translation reaction, the expressed SPNS2 was directly inserted into the lipid bilayer of the forming liposome. The SPNS2 proteoliposome complexes were isolated by centrifugation. Briefly, to prepare plasmid DNA templates the coding region of *SPNS2* from Human Tagged ORF Clone in pCMV6-AC-GFP (#RG225940, Origene) was inserted into the expression vector pEU-E01-MCS. Plasmid DNA template was isolated from transformed NEB 5-alpha E. coli (# C2987H, New England Biolabs) in LB broth with 100 µg/mL ampicillin (#L8105, Teknova) with the Monarch Plasmid Miniprep Kit (#T1010S, New England Biolabs) and further purified with Monarch PCR & DNA Cleanup Kit (#T1030S, New England Biolabs). Elution was performed with nuclease-free water. DNA purity was assessed by measuring the A260/A280 ratio. Plasmid DNA (1 µg/ µl) was used as a template for in vitro transcription. 2 µl plasmid DNA was added to 18 µl of Transcription Premix LM solution containing RNA polymerase SP6, ribonucleotide triphosphates (ATP, GTP, CTP, UTP), DTT, Mg(OAc)$_2$, spermidine, glycerol, and Triton X-100 in HEPES buffer (pH 8.0) and transcription reaction mixture was incubated at 37 °C for 1 h to synthesize *SPNS2* or control mRNA. To protect the newly synthesized mRNA from degradation, ribonuclease inhibitors are also included.

For the translation reaction by the bilayer method, the vial with 21 µl pre-mixed WEPRO®9 L solution containing wheat germ extract, creatine kinase and creatine phosphate, KOAc and Asolectin lipids from soybean in HEPES buffer was spun down to collect the reagents at the bottom of the vial and glucose (1 µM) or S1P (1 µM) was added and gently mixed together with 9 µl of the Transcription Premix LM solution containing *SPNS2* or control synthesized mRNA described above. This translation mixture (30 µl) was carefully transferred under 210 µl of the high-performance translation SUB-AMIX®SGC solution to form a bilayer. This setup, with two distinct layers that do not initially mix, maintains a gradient, allowing the spontaneous assembly of proteoliposomes as translation proceeds at the interface between the two layers. The mixture was incubated at room temperature for 20 h. The resulting proteoliposomes were isolated by centrifugation at 21,400 × *g* for 20 min at 4 °C and resuspended in PBS for measurement of glucose and S1P transporter activities.

To determine loading of the liposomes with glucose or S1P encapsulated within the liposome's aqueous core during these steps, similar reactions were carried out without mRNA in the presence of 1 µM NBD-glucose or 1 µM NBD-S1P and loading confirmed by NBD fluorescence measurements. In vitro transcription and translation reactions were also carried out with pEU-E01-T1R1 expression vector to prepare control T1R1 proteoliposomes.

SPNS2 proteoliposome in vitro transport assays

15 µL of proteoliposomes containing SPNS2 or SPNS2 mutants prepared as described above were added into 45 µL of assay buffer (20 mM HEPES and 150 mM NaCl at pH 7.5). S1P transport was initiated by addition of 1 µM NBD-S1P. Glucose transport was initiated with 1 µM NBD-glucose. The transport assays were stopped after 10 min by adding 1 ml cold assay buffer and excess ligands removed by washing and centrifugation of the proteoliposomes in cold assay buffer three times. Uptake of NBD-S1P or NBD-glucose was determined by fluorescence measured at an excitation of 467 nm and emission at 539 nm with a TECAN Infinite M1000 fluorescence plate reader.

[^{3}H]Glucose uptake by SPNS2 proteoliposomes

Time course and kinetics of [^{3}H]glucose uptake in SPNS2 proteoliposome assays was carried out as described for GLUT transporters with minor modifications[51,52]. For time course experiments, uptake was started by adding [^{3}H]glucose (Deoxy D-Glucose [1,2-^{3}H(N)], 5.4 Ci/mmol, 1 uCi/µl in water, from Moravek Inc., Brea, CA) together with 200 µM unlabeled D-glucose to 15 µl SPNS2 proteoliposomes prepared as described above in Methods. Transport was stopped at the indicated times with 200 µl of ice-cold quench buffer (50 mM potassium phosphate, pH 7.4, 130 mM KCl, pH 7.4) and then filtered by vacuum on a 0.22-µm mixed cellulose esters membrane filter (#GSTF02500, Millipore). Filters were subsequently washed with an additional 1 ml of quench buffer. Scintillation fluid was added to the filters and the radioactivity counted. For kinetic analyses, the ratio of [^{3}H]glucose and unlabeled glucose was kept constant (1:200) for the entire experiment while increasing the total glucose concentration. Specific uptake was calculated for all experiments by subtraction of nonspecific [^{3}H]glucose uptake by empty liposomes. Subtracted values were normalized to the amount of SPNS2 per assay. Values were fitted by non-linear regression analysis using GraphPad Prism 6.0. to Michaelis–Menten kinetics, and K_m, V_{max}, and k_{cat} were calculated. The amount of SPNS2 used in uptake assays was determined by analyzing aliquots of SPNS2 proteoliposomes alongside with a western blot standard curve and quantified with the Azure 600 imaging system (Azure Biosystems, USA).

Statistical analyses

All biochemical data were from biological replicates. Data are representative of at least three independent experiments. All *n* values represent individual biological replicates, while N is the number of independent experiments. Statistical significances were determined with an unpaired two-tailed Student *t* test for comparison of two groups or by ANOVA for multiple comparisons followed by post hoc tests to examine interactions between multiple variables using GraphPad Prism 7.0 software (San Diego, Calif). All datasets were analyzed for outliers by ROUT ($Q = 1\%$), and for normality by Shapiro–Wilk statistical test. Normality-passed datasets were compared by unpaired, two-tailed t-test. Datasets with a failed normality test were compared by unpaired, two-tailed Mann-Whitney test. Data are presented as mean ± SEM, $p < 0.05$ was statistically significant. No statistical methods were used to predetermine sample size.

Reporting summary

Further information on research design is available in the Nature Portfolio Reporting Summary linked to this article.

Data availability

All data is available in the main text or the supplementary materials. M.D. simulation trajectory files were deposited at https://zenodo.org/records/18765542. Source data are provided with this paper. Simulation parameters and validation criteria are summarized in Supplementary Table 4. The structure of SPNS2 in Fig. 6g was created using 3D Protein Imager[87]. Plasmids and cell lines can be requested from, and requests will be fulfilled by Dr. Cynthia Weigel.

References

1. Spiegel, S., Maczis, M. A., Maceyka, M. & Milstien, S. New insights into functions of the sphingosine-1-phosphate transporter SPNS2. *J. Lipid Res.* **60**, 484–489 (2019).
2. Kowalski, G. M., Carey, A. L., Selathurai, A., Kingwell, B. A. & Bruce, C. R. Plasma sphingosine-1-phosphate is elevated in obesity. *PLoS One* **8**, e72449 (2013).
3. Guitton, J. et al. Sphingosine-1-phosphate metabolism in the regulation of obesity/type 2 diabetes. *Cells* **9**, 1682 (2020).
4. Green, C. D., Maceyka, M., Cowart, L. A. & Spiegel, S. Sphingolipids in metabolic disease: the good, the bad, and the unknown. *Cell Metab.* **33**, 1293–1306 (2021).
5. Drew, D., North, R. A., Nagarathinam, K. & Tanabe, M. Structures and general transport mechanisms by the major facilitator superfamily (MFS). *Chem. Rev.* **121**, 5289–5335 (2021).
6. Fukuhara, S. et al. The sphingosine-1-phosphate transporter Spns2 expressed on endothelial cells regulates lymphocyte trafficking in mice. *J. Clin. Invest.* **122**, 1416–1426 (2012).
7. Okuniewska, M. et al. SPNS2 enables T cell egress from lymph nodes during an immune response. *Cell Rep.* **36**, 109368 (2021).
8. Baeyens, A. et al. Monocyte-derived S1P in the lymph node regulates immune responses. *Nature* **592**, 290–295 (2021).
9. Tanaka, S. et al. Sphingosine 1-phosphate signaling in perivascular cells enhances inflammation and fibrosis in the kidney. *Sci. Transl. Med.* **14**, *eabj2681* (2022).
10. van der Weyden, L. et al. Genome-wide in vivo screen identifies novel host regulators of metastatic colonization. *Nature* **541**, 233–236 (2017).
11. Chen, J. et al. Spinster homolog 2 (spns2) deficiency causes early onset progressive hearing loss. *PLoS Genet.* **10**, e1004688 (2014).
12. Donoviel, M. S. et al. Spinster 2, a sphingosine-1-phosphate transporter, plays a critical role in inflammatory and autoimmune diseases. *FASEB J.* **29**, 5018–5028 (2015).
13. Jumper, J. et al. Highly accurate protein structure prediction with AlphaFold. *Nature* **596**, 583–589 (2021).
14. Chen, H. et al. Structural and functional insights into Spns2-mediated transport of sphingosine-1-phosphate. *Cell* **186**, 2644–2655 (2023).
15. Duan, Y. et al. Structural basis of Sphingosine-1-phosphate transport via human SPNS2. *Cell Res.* **34**, 177–180 (2024).
16. Pang, B. et al. Molecular basis of Spns2-facilitated sphingosine-1-phosphate transport. *Cell Res.* **34**, 173–176 (2024).
17. Tang, H. et al. The solute carrier SPNS2 recruits PI(4,5)P(2) to synergistically regulate transport of sphingosine-1-phosphate. *Mol. Cell* **83**, e2735 (2023).
18. Yariv, B. et al. Using evolutionary data to make sense of macromolecules with a “face-lifted” ConSurf. *Protein Sci.* **32**, e4582 (2023).
19. Mendoza, A. et al. The transporter Spns2 is required for secretion of lymph but not plasma sphingosine-1-phosphate. *Cell Rep.* **2**, 1104–1110 (2012).
20. Sala-Rabanal, M. et al. Revisiting the physiological roles of SGLTs and GLUTs using positron emission tomography in mice. *J. Physiol.* **594**, 4425–4438 (2016).
21. Blanchard, O. et al. Downregulation of the S1P transporter spinster homology protein 2 (Spns2) exerts an anti-fibrotic and anti-inflammatory effect in human renal proximal tubular epithelial cells. *Int. J. Mol. Sci.* **19**, 1498 (2018).
22. Hisano, Y., Kobayashi, N., Yamaguchi, A. & Nishi, T. Mouse SPNS2 functions as a sphingosine-1-phosphate transporter in vascular endothelial cells. *PLoS One* **7**, e38941 (2012).
23. Nagahashi, M. et al. Spns2, a transporter of phosphorylated sphingoid bases, regulates their blood and lymph levels, and the lymphatic network. *FASEB J.* **27**, 1001–1011 (2013).
24. Ohtoyo, M. et al. Component of caramel food coloring, THI, causes lymphopenia indirectly via a key metabolic intermediate. *Cell Chem. Biol.* **23**, 555–560 (2016).
25. Fritzemeier, R. et al. Discovery of in vivo active sphingosine-1-phosphate transporter (Spns2) Inhibitors. *J. Med Chem.* **65**, 7656–7681 (2022).
26. Rapizzi, E. et al. Sphingosine 1-phosphate increases glucose uptake through trans-activation of insulin receptor. *Cell Mol. Life Sci.* **66**, 3207–3218 (2009).
27. Yanagida, K. & Hla, T. Vascular and immunobiology of the circulatory sphingosine 1-phosphate gradient. *Annu. Rev. Physiol.* **79**, 67–91 (2017).
28. Weigel, C., Bellaci, J. & Spiegel, S. Sphingosine-1-phosphate and its receptors in vascular endothelial and lymphatic barrier function. *J. Biol. Chem.* **299**, 104775 (2023).
29. Kunkel, G. T., Maceyka, M., Milstien, S. & Spiegel, S. Targeting the sphingosine-1-phosphate axis in cancer, inflammation and beyond. *Nat. Rev. Drug Discov.* **12**, 688–702 (2013).
30. Thorens, B. & Mueckler, M. Glucose transporters in the 21st century. *Am. J. Physiol. Endocrinol. Metab.* **298**, E141–E145 (2010).
31. Wu, W. Z. & Bai, Y. P. Endothelial GLUTs and vascular biology. *Biomed. Pharmacother.* **158**, 114151 (2023).
32. Wu, D. et al. Single-cell metabolic imaging reveals a SLC2A3-dependent glycolytic burst in motile endothelial cells. *Nat. Metab.* **3**, 714–727 (2021).
33. Lee, E. E. et al. A protein kinase C phosphorylation motif in GLUT1 affects glucose transport and is mutated in GLUT1 deficiency syndrome. *Mol. Cell* **58**, 845–853 (2015).
34. Mamun, A. A., Hayashi, H., Yamamura, A., Nayeem, M. J. & Sato, M. Hypoxia induces the translocation of glucose transporter 1 to the plasma membrane in vascular endothelial cells. *J. Physiol. Sci.* **70**, 44 (2020).
35. Holman, G. D. Structure, function and regulation of mammalian glucose transporters of the SLC2 family. *Pflug. Arch.* **472**, 1155–1175 (2020).
36. Olszewski, K. et al. Inhibition of glucose transport synergizes with chemical or genetic disruption of mitochondrial metabolism and suppresses TCA cycle-deficient tumors. *Cell Chem. Biol.* **29**, e410 (2022).
37. Hamill, S., Cloherty, E. K. & Carruthers, A. The human erythrocyte sugar transporter presents two sugar import sites. *Biochemistry* **38**, 16974–16983 (1999).
38. Thomas, N. et al. Sphingosine-1-phosphate suppresses GLUT activity through PP2A and counteracts hyperglycemia in diabetic red blood cells. *Nat. Commun.* **14**, 8329 (2023).

39. Xie, T. et al. Erythrocyte metabolic reprogramming by sphingosine 1-phosphate in chronic kidney disease and therapies. *Circ. Res* **127**, 360–375 (2020).
40. Tumova, S., Kerimi, A., Porter, K. E. & Williamson, G. Transendothelial glucose transport is not restricted by extracellular hyperglycaemia. *Vasc. Pharm.* **87**, 219–229 (2016).
41. Jeya Paul, J. et al. Inflammatory conditions disrupt constitutive endothelial cell barrier stabilization by alleviating autonomous secretion of sphingosine 1-phosphate. *Cells* **9**, 928 (2020).
42. Li, H. Z. et al. Transport and inhibition of the sphingosine-1-phosphate exporter SPNS2. *Nat. Commun.* **16**, 721 (2025).
43. Harder, D. & Fotiadis, D. Measuring substrate binding and affinity of purified membrane transport proteins using the scintillation proximity assay. *Nat. Protoc.* **7**, 1569–1578 (2012).
44. Chatzikyriakidou, Y., Ahn, D. H., Nji, E. & Drew, D. The GFP thermal shift assay for screening ligand and lipid interactions to solute carrier transporters. *Nat. Protoc.* **16**, 5357–5376 (2021).
45. Alexandrov, A. I., Mileni, M., Chien, E. Y., Hanson, M. A. & Stevens, R. C. Microscale fluorescent thermal stability assay for membrane proteins. *Structure* **16**, 351–359 (2008).
46. Kotov, V. et al. In-depth interrogation of protein thermal unfolding data with MoltenProt. *Protein Sci.* **30**, 201–217 (2021).
47. Zhou, F. et al. Crystal structure of a bacterial homolog to human lysosomal transporter, spinster. *Sci. Bull.* **64**, 1310–1317 (2019).
48. Kawahara, A. et al. The sphingolipid transporter spns2 functions in migration of zebrafish myocardial precursors. *Science* **323**, 524–527 (2009).
49. Kuruma, Y. & Ueda, T. The PURE system for the cell-free synthesis of membrane proteins. *Nat. Protoc.* **10**, 1328–1344 (2015).
50. Amati, A. M., Graf, S., Deutschmann, S., Dolder, N. & von Ballmoos, C. Current problems and future avenues in proteoliposome research. *Biochem. Soc. Trans.* **48**, 1473–1492 (2020).
51. Hresko, R. C., Kraft, T. E., Quigley, A., Carpenter, E. P. & Hruz, P. W. Mammalian glucose transporter activity is dependent upon anionic and conical phospholipids. *J. Biol. Chem.* **291**, 17271–17282 (2016).
52. Suades, A. et al. Establishing mammalian GLUT kinetics and lipid composition influences in a reconstituted-liposome system. *Nat. Commun.* **14**, 4070 (2023).
53. Henderson, R. K., Fendler, K. & Poolman, B. Coupling efficiency of secondary active transporters. *Curr. Opin. Biotechnol.* **58**, 62–71 (2019).
54. Cartier, A. & Hla, T. Sphingosine 1-phosphate: lipid signaling in pathology and therapy. *Science* **366**, eaar5551 (2019).
55. Fu, P. et al. Role of sphingosine kinase 1 and S1P transporter Spns2 in HGF-mediated lamellipodia formation in lung endothelium. *J. Biol. Chem.* **291**, 27187–27203 (2016).
56. Geng, X. et al. S1PR1 regulates lymphatic valve development and tertiary lymphoid organ formation in the ileum. *J. Exp. Med.* **222**, e20241799 (2025).
57. Zheng, S. et al. Microbiota-derived imidazole propionate inhibits type 2 diabetic skin wound healing by targeting SPNS2-mediated S1P transport. *iScience* **26**, 108092 (2023).
58. Kharel, Y. et al. Assessment of Spinster homologue 2 (Spns2)-dependent transport of sphingosine-1-phosphate as a therapeutic target. *Br. J. Pharm.* **182**, 2014–2030 (2025).
59. Takabe, K., Paugh, S. W., Milstien, S. & Spiegel, S. "Inside-out" signaling of sphingosine-1-phosphate: therapeutic targets. *Pharmacol. Rev.* **60**, 181–195 (2008).
60. Akhter, M. Z. et al. Programming to S1PR1(+) endothelial cells promotes restoration of vascular integrity. *Circ. Res.* **129**, 221–236 (2021).
61. Li, M. et al. Sphingosine-1-phosphate transporter spinster homolog 2 is essential for iron-regulated metastasis of hepatocellular carcinoma. *Mol. Ther.* **30**, 703–713 (2022).
62. Del Gaudio, I. et al. Endothelial Spns2 and ApoM regulation of vascular tone and hypertension via sphingosine-1-phosphate. *J. Am. Heart Assoc.* **10**, e021261 (2021).
63. Mina, A. I. et al. CalR: a web-based analysis tool for indirect calorimetry experiments. *Cell Metab.* **28**, e651 (2018).
64. Sala-Rabanal, M. et al. Intestinal absorption of glucose in mice as determined by positron emission tomography. *J. Physiol.* **596**, 2473–2489 (2018).
65. Weigel, C. et al. Sphingosine kinase 2 in stromal fibroblasts creates a hospitable tumor microenvironment in breast cancer. *Cancer Res.* **83**, 553–567 (2023).
66. Ando, T. et al. Isolation and characterization of a novel mouse lymphatic endothelial cell line: SV-LEC. *Lymphat. Res. Biol.* **3**, 105–115 (2005).
67. Andersen, C. L., Jensen, J. L. & Orntoft, T. F. Normalization of real-time quantitative reverse transcription-PCR data: a model-based variance estimation approach to identify genes suited for normalization, applied to bladder and colon cancer data sets. *Cancer Res.* **64**, 5245–5250 (2004).
68. Pfaffl, M. W., Horgan, G. W. & Dempfle, L. Relative expression software tool (REST) for group-wise comparison and statistical analysis of relative expression results in real-time PCR. *Nucleic Acids Res.* **30**, e36 (2002).
69. Markwart, R. et al. Immunosuppression after sepsis: systemic inflammation and sepsis induce a loss of naive T-cells but no enduring cell-autonomous defects in T-cell function. *PLoS One* **9**, e115094 (2014).
70. Trott, O. & Olson, A. J. AutoDock Vina: improving the speed and accuracy of docking with a new scoring function, efficient optimization, and multithreading. *J. Comput. Chem.* **31**, 455–461 (2010).
71. Sanner, M. F. Python: a programming language for software integration and development. *J. Mol. Graph Model* **17**, 57–61 (1999).
72. Wu, E. L. et al. CHARMM-GUI Membrane Builder toward realistic biological membrane simulations. *J. Comput. Chem.* **35**, 1997–2004 (2014).
73. Jo, S., Kim, T., Iyer, V. G. & Im, W. CHARMM-GUI: a web-based graphical user interface for CHARMM. *J. Comput Chem.* **29**, 1859–1865 (2008).
74. van Meer, G., Voelker, D. R. & Feigenson, G. W. Membrane lipids: where they are and how they behave. *Nat. Rev. Mol. Cell Biol.* **9**, 112–124 (2008).
75. Lorent, J. H. et al. Plasma membranes are asymmetric in lipid unsaturation, packing and protein shape. *Nat. Chem. Biol.* **16**, 644–652 (2020).
76. Jorgensen, W. L., Chandrasekhar, J., Madura, J. D., Impey, R. W. & Klein, M. L. Comparison of simple potential functions for simulating liquid water. *J. Chem. Phys.* **79**, 926–935 (1983).
77. Martyna, G. J., Tobias, D. J. & Klein, M. L. Constant pressure molecular dynamics algorithms. *J. Chem. Phys.* **101**, 4177–4189 (1994).
78. Feller, S. E., Zhang, Y., Pastor, R. W. & Brooks, B. R. Constant pressure molecular dynamics simulation: the Langevin piston method. *J. Chem. Phys.* **103**, 4613–4621 (1995).
79. Ryckaert, J.-P., Ciccotti, G. & Berendsen, H. J. Numerical integration of the cartesian equations of motion of a system with constraints: molecular dynamics of n-alkanes. *J. Comput. Phys.* **23**, 327–341 (1977).
80. Essmann, U. et al. A smooth particle mesh Ewald method. *J. Chem. Phys.* **103**, 8577–8593 (1995).
81. Darden, T., York, D. & Pedersen, L. Particle mesh Ewald: an N· log (N) method for Ewald sums in large systems. *J. Chem. Phys.* **98**, 10089–10092 (1993).
82. Phillips, J. C. et al. Scalable molecular dynamics with NAMD. *J. Comput. Chem.* **26**, 1781–1802 (2005).
83. Kumar, S., Rosenberg, J. M., Bouzida, D., Swendsen, R. H. & Kollman, P. A. The weighted histogram analysis method for free-energy

calculations on biomolecules. I. The method. *J. Comput. Chem.* **13**, 1011–1021 (1992).
84. Humphrey, W., Dalke, A. & Schulten, K. VMD: visual molecular dynamics. *J. Mol. Graph* **14**, 27–38 (1996).
85. Sauer, D. et al. Transport and inhibition of the sphingosine-1-phosphate exporter SPNS2. *Nat. Commun*. 16, 721 (2023).
86. Nishiguchi, R. et al. Evaluation of cell-free synthesized human channel proteins for in vitro channel research. *Membranes* **13**, 48 (2022).
87. Tomasello, G., Armenia, I. & Molla, G. The Protein Imager: a full-featured online molecular viewer interface with server-side HQ-rendering capabilities. *Bioinformatics* **36**, 2909–2911 (2020).

Acknowledgements

This work was supported by the National Institutes of Health under Grant R35GM152058 (S.S.). We thank Drs. Martin Mangino, Javier González Maeso, Jason Younkin, Barbara Fujita, Jolene Windle, Mark Subler, Jennifer Koblinski, and Vita Kraskauskiene from VCU School of Medicine, and Rebecca Heise from VCU, Department of Biomedical Engineering, for providing instrumentation and expertise. The authors acknowledge the Virginia Commonwealth University Lipidomics/Metabolomics, Tissue and Data Acquisition and Analysis, Flow Cytometry, Bioimaging and Applied Research Core and Microscopy Shared Resources, which are supported in part by funding from the NIH-NCI Cancer Center Support Grant P30 CA016059. D.B.S. was supported by the EUbOpen project under grant agreement no. 875510. H.Z.L. was supported by the RESOLUTE project under grant agreement no. 777372.

Author contributions

C.W. designed and performed the experiments with cells and animals, analyzed the data and wrote the manuscript; M.L.H. and P.P.C. carried out the simulation studies; E.N.D.P., S.S., and R.D.R.B. performed confocal microscopy; R.D.R.B performed quantitative RT-PCR. C.G. helped with WB analyses; J.N. helped with blood analyses; B.N and F.S.C provided expertise for metabolic phenotyping; F.C. and C.W. performed PET scanning; C.S., H.Z.L, and D.B.S purified proteins; X.F. provided critical reagents and helped with radiometric assays. S.S. supervised the study, provided advice, helped with data analysis, designed the experiments, analyzed the data, and wrote the manuscript.

Competing interests

The authors declare no competing interests.

Additional information

Supplementary information The online version contains supplementary material available at https://doi.org/10.1038/s41467-026-71659-7.

Correspondence and requests for materials should be addressed to Cynthia Weigel or Sarah Spiegel.

Peer review information *Nature Communications* thanks the anonymous reviewer(s) for their contribution to the peer review of this work. A peer review file is available.

Reprints and permissions information is available at http://www.nature.com/reprints